APLICAÇÕES DE PROCESSAMENTO DE SINAIS DE ARRANJOS EM ENGENHARIA BIOMÉDICA

ELENA JAVIDI DA COSTA

TESE DE DOUTORADO EM SISTEMAS MECATRÔNICOS

DEPARTAMENTO DE ENGENHARIA MECÂNICA

FACULDADE DE TECNOLOGIA

UNIVERSIDADE DE BRASÍLIA

UNIVERSIDADE DE BRASÍLIA
FACULDADE DE TECNOLOGIA
DEPARTAMENTO DE ENGENHARIA MECÂNICA

APLICAÇÕES DE PROCESSAMENTO DE SINAIS DE ARRANJOS EM ENGENHARIA BIOMÉDICA

ARRAY SIGNAL PROCESSING APPLICATIONS ON BIOMEDICAL ENGINEERING

ELENA JAVIDI DA COSTA

ORIENTADOR: JOSÉ ALFREDO RUIZ VARGAS, PROF. DR.
COORIENTADOR: GIOVANNI ALMEIDA SANTOS, PROF. DR.

TESE DE DOUTORADO EM SISTEMAS MECATRÔNICOS

BRASÍLIA/DF: JANEIRO - 2024

UNIVERSIDADE DE BRASÍLIA
FACULDADE DE TECNOLOGIA
DEPARTAMENTO DE ENGENHARIA MECÂNICA

APLICAÇÕES DE PROCESSAMENTO DE SINAIS DE ARRANJOS EM ENGENHARIA BIOMÉDICA

ELENA JAVIDI DA COSTA

TESE DE DOUTORADO SUBMETIDA AO DEPARTAMENTO DE ENGENHARIA MECÂNICA DA FACULDADE DE TECNOLOGIA DA UNIVERSIDADE DE BRASÍLIA COMO PARTE DOS REQUISITOS NECESSÁRIOS PARA A OBTENÇÃO DO GRAU DE DOUTOR.

APROVADA POR:

_____

Prof. Dr. José Alfredo Ruiz Vargas – ENE/UnB
Presidente

_____

Prof. Dr. Ricardo Zelenovsky – ENE/UnB
Examinador Interno

_____

Prof. Dr. Edison Pignaton de Freitas – UFRGS
Examinador Externo

_____

Prof. Dr. Ebrahim Samer El youssef – UFSC
Examinador Externo

BRASÍLIA, 22 DE JANEIRO DE 2024.

FICHA CATALOGRÁFICA

DA COSTA, ELENA J.
Aplicações de Processamento de Sinais de Arranjos em Engenharia Biomédica [Distrito Federal] 2024.
xiv, 64p., 210 x 297 mm (ENM/FT/UnB, Doutor, Sistemas Mecatrônicos, 2024).
Tese de Doutorado – Universidade de Brasília, Faculdade de Tecnologia.
Departamento de Engenharia Mecânica

1.	2.
3.	4.
I. ENM/FT/UnB	II. Título (série)

REFERÊNCIA BIBLIOGRÁFICA

DA COSTA, E. J. (2024). Aplicações de Processamento de Sinais de Arranjos em Engenharia Biomédica. Tese de Doutorado em Sistemas Mecatrônicos, Publicação , Departamento de Engenharia Mecânica, Universidade de Brasília, Brasília, DF, 64p.

CESSÃO DE DIREITOS

AUTOR: Elena Javidi da Costa
TÍTULO: Aplicações de Processamento de Sinais de Arranjos em Engenharia Biomédica.
GRAU: Doutor ANO: 2024

Elena Javidi da Costa

Departamento de Engenharia Mecânica (ENM) - FT
Universidade de Brasília (UnB)
Campus Darcy Ribeiro
CEP 70919-970 - Brasília - DF - Brasil

À minha filha Isabela

AGRADECIMENTOS

Agradeço imensamente o conhecimento compartilhado e a orientação dedicada do Prof. José Alfredo Ruiz Vargas e do Prof. Giovanni Almeida Santos. Também agradeço aos colegas Dr. Ricardo Kehrle Miranda, Dr. João Paulo Abreu Maranhão e Antonio Arlis Santos da Silva pelo apoio na pesquisa.
Também agradeço imensamente aos membros da minha banca, Prof. Ricardo Zelenovsky, Prof. Edison Pignaton de Freitas e Prof. Ebrahim Samer El Youssel, pelos comentários para melhorar o texto deste tese.

Por fim, agradeço a minha família, cujo amor e encorajamento foram a força motriz por trás desta jornada acadêmica. Em particular, eu agradeço aos meus pais, Elaheh e Hassan, cujo apoio incansável sustentou meu caminho, à minha fonte de inspiração, minha filha Isabela, e ao meu marido João Paulo pelo amor e compreensão ao longo desta jornada.

RESUMO

Título: Array Signal Processing Applications on Biomedical Engineering
Autor: Elena Javidi da Costa
Orientador: José Alfredo Ruiz Vargas, Prof. Dr.
Coorientador: Giovanni Almeida Santos, Prof. Dr.
Programa de Pós-Graduação em Sistemas Mecatrônicos
Brasília, 22 de janeiro de 2024

Nesta tese, soluções de hardware e software para aplicações em engenharia biomédica são propostas. Em particular, técnicas baseadas em processamento de sinais adquiridos com arranjos de sensores são consideradas. Primeiro, é proposto um dispositivo de saúde com vários sensores, do inglês *Multi-sensor Wearable Health Device* (MWHD), incluindo algoritmos de processamento de sinais de alta resolução para medir a freqüência cardíaca e a quantidade de passos. Em seguida, é apresentada uma modificação dos Critérios Teóricos de Informação, do inglês *Information Theoretic Criteria* (ITC), tradicionais baseados em autovalores, a fim de estimar a quantidade de componentes de medições de Magnetoencefalografia, do inglês *Magnetoencephalography* (MEG), e Eletroencefalografia, do inglês *Electroencephalography* (EEG). Finalmente, é desenvolvida uma estrutura não supervisionada para a identificação do Potencial Evocado Visual, do inglês *Visual Evoked Potential* (VEP), nas medições de MEG. As técnicas propostas foram validadas através de medições. Ao longo do desenvolvimento desta pesquisa, contribuições adicionais nas áreas de segurança cibernética, contagem de passos e localização de drones foram proporcionadas, as quais encontram-se detalhadas nos apêndices.

Palavras-chave: Multi-sensor, MEG, Seleção da Ordem do Modelo, VEP

ABSTRACT

Title: Aplicações de Processamento de Sinais de Arranjos em Engenharia Biomédica
Author: Elena Javidi da Costa
Supervisor: José Alfredo Ruiz Vargas, Prof. Dr.
Co-Supervisor: Giovanni Almeida Santos, Prof. Dr.
Post-Graduate Program in Mechatronic Systems
Brasília, Jan 22nd, 2024

In this thesis, hardware and software solutions for biomedical engineering applications are proposed. In particular, the development of techniques based on array signal processing is considered. First, a MWHD, including high-resolution signal processing algorithms to measure of the *Heart Rate* (HR) and the steps, is proposed. Next, a novel modification of the traditional eigenvalue based ITC is presented in order to estimate the amount of components of MEG and EEG data. Finally, an unsupervised framework for the identification of VEP in MEG measurements is developed. The proposed approaches are validated using measurements. Throughout the development of this research, additional contributions in the areas of cybersecurity, step counting, and drone localization have been provided, which are detailed in the appendices.

Keywords: Multi-sensor, MEG, Model Order Selection, VEP

SUMMARY

1 INTRODUCTION 1

1.1 MOTIVATION 1

1.2 OBJECTIVES 2

1.3 CONTRIBUTIONS OF THIS WORK 2

1.4 OVERALL ORGANIZATION 3

2 MULTI-SENSOR WEARABLE HEALTH DEVICE FRAMEWORK 4

2.1 INTRODUCTION 4

2.2 STATE OF THE ART 5

2.2.1 STATE-OF-THE-ART SIMPLIFIED MODEL FOR PPG WAVEFORMS 6

2.3 PROPOSED HEALTHCARE PLATFORM COMPOSED OF LOW-COST HARDWARE, HIGH-RESOLUTION PARAMETER ESTIMATION ALGORITHMS AND REAL-TIME MONITORING APPLICATION ARCHITECTURE 7

2.3.1 PROPOSED HEALTHCARE WEARABLE DEVICE INCLUDING MULTIPLE SENSORS, PROCESSOR AND LOW ENERGY WIRELESS COMMUNICATION 8

2.3.2 PROPOSED HIGH RESOLUTION SIGNAL PROCESSING ALGORITHM FOR HR ESTIMATION 10

2.3.3 HEALTHCARE PLATFORM FOR REAL-TIME MONITORING AND EVALUATION 12

2.4 EXPERIMENTAL VALIDATION 14

2.5 SUMMARY OF THE CHAPTER 19

3 IDENTIFICATION OF VISUAL EVOKED POTENTIAL IN MEASUREMENTS 20

3.1 INTRODUCTION 20

3.2 OVERVIEW OF THE PROPOSED FRAMEWORK FOR VEP IDENTIFICATION 22

3.3 STATE-OF-THE-ART APPROCHES FOR THE ESTIMATION OF THE AMOUNT OF COMPONENTS 24

3.3.1 ESTIMATION OF THE AMOUNT OF COMPONENTS BY VISUAL INSPECTION VIA ICASSO 25

3.3.2 ESTIMATION OF THE AMOUNT OF COMPONENTS VIA ITC 26

3.4 PROPOSED MODIFIED APPROACHES FOR THE ESTIMATION OF THE AMOUNT OF COMPONENTS 28

3.4.1 ESTIMATION OF THE AMOUNT OF COMPONENTS COMBINING *Fast Inpedendent Component Analysis* (FASTICA) WITH ITC 28

3.4.2 Estimation of components of the sample covariance matrix using the modified ITC approaches 29
3.5 Experimental Results 30
3.5.1 Comparing schemes in terms of estimation of the amount of components 30
3.5.2 Comparing schemes in terms of procesing time 33
3.6 Summary of the Low complexity modified AIC 33
3.7 Proposed unsupervised framework for the VEP identification ... 34
3.7.1 Calibration scheme to determine the threshold value τ ... 35
3.7.2 Unsupervised identification using the calibration parameter τ 35
3.7.3 Subjective VEP identification via visual inspection 36
3.7.4 Decision fusion based on the outputs of all approaches 37
3.8 Experimental Results 37
3.8.1 Calculation and validation of τ parameter 37
3.8.2 Automatic unsupervised VEP identification 39
3.8.3 Subjective VEP Identification via Visual Inspection 41
3.8.4 Decision fusion based on the outputs of all approaches 44
3.9 Summary of the chapter 45

4 CONCLUSIONS 46

BIBLIOGRAPHY 46

A CYBERSECURTIY FRAMEWORK 55

B ALGORITHMS OF THE MULTI-SENSOR HEALTH WEARABLE DEVICE FRAMEWORK 58

C STEP COUNTER 61

D DRONE LOCALIZATION IN MULTIPATH ENVIRONMENTS 63

LIST OF FIGURES

2.1 Diagram of the proposed healthcare framework, consisting of a multi-sensor health wearable device, *Photoplethysmography* (PPG) high resolution parameter estimation and real-time monitoring application. 7
2.2 Block diagram showing the functional circuit components of the proposed prototype wristband. 8
2.3 Dimensions of the PCB and enclosure produced for the proposed MWHD device prototype. 10
2.4 Software architecture for the developed real-time monitoring healthcare application. 13
2.5 *Root-Mean-Square-Error* (RMSE) of estimated *Beats-per-Minute* (BPM) values for each algorithm for different current level configurations, referenced to values read by the oximeter. 16
2.6 RMSE of estimated BPM values for each algorithm for different current level configurations, referenced to values read by the smartband. 16
2.7 RMSE of estimated BPM values for different pulse width and corresponding *Analog-to-Digital Converter* (ADC) resolution configurations, referenced to values read by the oximeter. 17
2.8 RMSE of estimated BPM values for each algorithm for different pulse width and corresponding ADC resolution configurations, referenced to values read by the smartband. 17

3.1 Proposed framework for model order selection and unsupervised identification of visually evoked potential components 22
3.2 Measurement device Elekta Neuromag with flicker stimulation in the Biomagnetic Center at the Jena University Hospital 23
3.3 Data Structure 23
3.4 Estimation of the amount of components using ICASSO similarity plot of block frequency at $f_{s_1} = 3.84$ Hz of the first volunteer. 26
3.5 Estimation amount of components using the state-of-the-art ITC shown in Subsection 3.3.2 using the main diagonal of the matrix $(\mathbf{\Sigma}_X)$ of the measurements of block frequency at 3.84 Hz of the first volunteer. 31
3.6 Estimation of the amount of components using the state-of-the-art ITC shown in Subsection 3.3.2 using the main diagonal of the matrix $(\mathbf{\Sigma}_A)(1 : I_{max})$ of the measurements of block frequency at 3.84 Hz of the first volunteer. 31

3.7 Estimation of the amount of components using the state-of-the-art ITC shown in Subsection 3.3.2 using the main diagonal of the matrix $(\mathbf{\Sigma}_X)(1 : I_{max})$ of the measurements of block frequency at 3.84 Hz of the first volunteer..... 32
3.8 Histogram of the $\phi^n_{p,\text{min}}$ obtained from Equation (3.22). Note that $\tau \approx 0.6$ for the data without stimulation 38
3.9 Histogram of the $\phi^n_{p,\text{min}}$ obtained from Equation (3.22). Note that $\tau \approx 0.5$ for the data without stimulation 39
3.10 Histogram of the $\phi^s_{p,\text{min}}$ obtained from Equation (3.25). Note that $\tau \approx 0.7$ for the data with stimulation..... 40
3.11 Histogram of the $\phi^s_{p,\text{min}}$ obtained from Equation (3.25). Note that $\tau \approx 0.85$ for the data with stimulation 41
3.12 Mean value of the amplitude spectrum of the independent component with $p = 2$ considering a stimulation $f_{s1} = 3.84$ Hz. Note that the independent component with $p = 2$ can be identified as VEP using this criterion 42
3.13 Mean value of the amplitude spectrum of the independent component with $p = 6$ considering a stimulation $f_{s1} = 3.84$ Hz. Note that the independent component with $p = 2$ can be identified as VEP using this criterion 42
3.14 Spectral topography of the independent component with $p = 2$ considering a stimulation $f_{s1} = 3.84$ Hz. Note that the independent component with $p = 2$ cannot be identified as VEP using this criterion 43
3.15 Spectral topography of the independent component with $p = 6$ considering a stimulation $f_{s1} = 3.84$ Hz. Note that the independent component with $p = 6$ can be identified as VEP using this criterion..... 43

C.1 The proposed ESPRIT based approach for the estimation of the amount of steps outperforms the state-of-the-art schemes. 62

D.1 The proposed MuDe based approach for the estimation of the position outperforms the state-of-the-art schemes. 64

LIST OF TABLES

2.1 LED pulse width configurations tested and the correspondent ADC resolution. 17
2.2 Maximum available ADC resolution for each sample rate configuration tested. 18
2.3 Access times to different test requests performed to the *Application Programming Interface* (API) of the real-time monitoring application. 19

3.1 Estimated amount of components of measurements with and without stimulation of the first volunteer..... 30
3.2 Estimation of the amount of components of the MEG measurements via *Akaike Information Criterion* (AIC) and *Minimum Description Length* (MDL). 32
3.3 Estimation of the amount of components of the MEG measurements via *Efficient Detection Criterion* (EDC) and *Bayesian Information Criterion* (BIC).. 32
3.4 Comparison of the time processing for the proposed and state-of-the-art approaches 33
3.5 Indices of the identified VEP independent components using the three unsupervised approaches considering three stimulation frequencies, namely, f_{s1}, f_{s2}, and f_{s3} 40
3.6 Indices of the identified VEP independent components using two visual inspection approaches considering three stimulation frequencies, namely, f_{s1}, f_{s2}, and f_{s3}. Example of the decision fusion applying the intersection operation 44
3.7 Indices of the identified VEP independent components using the three unsupervised identification approaches and the intersection of the two visual inspection approaches considering three stimulation frequencies, namely, f_{s1}, f_{s2}, and f_{s3}. Example of the decision fusion applying the tree different intersection operations 45

LIST OF ACRONYMS AND ABBREVIATIONS

ADC *Analog-to-Digital Converter*. x, xii, 14, 16–18
AIC *Akaike Information Criterion*. xii, 20, 21, 27, 30, 32, 45
API *Application Programming Interface*. xii, 18, 19

BIC *Bayesian Information Criterion*. xii, 28, 31, 32
BLE *Bluetooth Low Energy*. 5, 7, 8, 19
BPM *Beats-per-Minute* . x, 5, 6, 15–17
BSS *Blind Source Separation*. 1, 6, 20, 21, 24–26, 45

DDoS *Distributed Denial of Service*. 55–57
DHT *Discrete Hilbert Transform*. 11

EDC *Efficient Detection Criterion*. xii, 27, 31, 32
EEG *Electroencephalography*. i, 1, 2, 46
EMG *Electromyography*. 1
EMI *Electromagnetic Interference* . 9
ESPRIT *Estimation of Signal Parameters by Rotational Invariance Techniques*. 10–12, 14, 15
EVD *Eigenvalue Decomposition*. 11, 12, 34

FastICA *Fast Inpedendent Component Analysis*. viii, 24, 25, 28, 33
FFT *Fast-Fourier Transform*. 6

GPIO *General Purpose Input/Output*. 8

HCO *Healthcare Organization*. 1
HOOI *Higher Order Orthogonal Iteration*. 57
HR *Heart Rate*. i, 2, 5–10, 12, 14, 15, 18, 19
HRV *Heart Rate Variability*. 6

I^2C *Inter-Integrated Circuit*. 8
IBI *Inter-Beat Intervals*. 6
ICA *Independent Component Analysis*. 21, 26
ICU *Intensive Care Units*. 4
IDS *Intrusion Detection Systems*. 55

IoT *Internet of Things*. 61
IR *Infrared*. 9, 15, 16
ITC *Information Theoretic Criteria*. i, viii–xi, 2, 21, 24, 26–33, 45, 46

JTAG *Joint Test Action Group*. 8, 9

LiPo *Lithium-Polymer*. 8, 9, 18
LOS *Line of Sight*. 63

MCU *Microcontroller Unit*. 8–10
MDL *Minimum Description Length*. xii, 21, 27, 30, 32, 45
MEG *Magnetoencephalography*. i, 2, 3, 20, 21, 45, 46
ML *Machine Learning*. 20, 55, 56
MOS *Model Order Selection*. 3, 46, 56
MuDe *Multiple Denoising*. 3, 56, 57, 63
MWHD *Multi-sensor Wearable Health Device*. i, 2, 3, 5, 7–10, 14, 15, 18, 19, 46

NLOS *Non Line of Sight*. 63

PCA *Principal Component Analysis*. 6
PCB *Printed Circuit Board* . 9
PPG *Photoplethysmography*. x, 5–7, 9, 10, 14, 15, 18
PWM *Pulse-Width Modulation*. 18

REST *Representational State Transfer*. 18
RF *Radiofrequency*. 8
RMSE *Root-Mean-Square-Error*. x, 6, 15–18

SNR *Signal-Noise Ratio*. 1
SVM *Support Vector Machine*. 6

TDoA *Time Difference of Arrival*. 63

UAVs *Unmanned Aerial Vehicles*. 63

VEP *Visual Evoked Potential*. i, ix, 2, 3, 20, 21, 25, 26, 30, 45, 46

WBAN *Wireless Body Area Network*. 1

1 INTRODUCTION

Signal processing techniques are crucial for biomedical engineering. The biomedical signals are usually degraded by artifacts and noise. Moreover, extracting the desirable information from biomedical signals is very challenging, since the signals may present a very low Signal-Noise Ratio (SNR) and may vary according to the health and to several other internal and external factors. In order to deal with these aspects, array signal processing plays a major role. By using an array of sensors, the array gain considerably increases the SNR. Moreover, the signals from the sensor array can be separated using Blind Source Separation (BSS) techniques allowing us to understand the signal properties, such as amount of signal sources, the localization and the extraction of their respective signals. Finally, the blindly separated signals can be used to observe patterns related to the health state of the patient. In this introduction, we present the motivation, the objectives, contributions, and overall organization of this work.

1.1 MOTIVATION

Health networked sensors, worn on the body or embedded in living environments, can gather rich information on our physical and mental health. By acquiring such information on a continual basis, by aggregating it, and by effectively mining it, a transformative change in the health care can be achieved allowing prognosis, prevention, and cure of diseases, overall management of health, personalization of treatments, reduction of the costs of health care and improvement of outcomes [1]. The state-of-the-art frameworks for remote health monitoring are composed of an architecture, namely, *Wireless Body Area Network* (WBAN) consisting of wearable sensors as the data acquisition unit, communication and networking, and application [2]. In the data acquisition layer, wearable sensors measure physiological biomarkers, such as EEG, skin temperature, respiratory rate, *Electromyography* (EMG), heart rate, blood pressure, oxygen saturation, and gait, including both posture and movements [1, 2]. The communication and networking layers are responsible for the data transmission from the sensors to a device called data aggregator or concentrator, as exemplified in [3], and also for the data transmission from the concentrator to an internet provider, such that the medical data is stored at the *Healthcare Organization* (HCO). In this work, we propose the development of software and hardware for biomedical engineering applications. In particular, we propose array signal processing techniques in order to further improve the performance of the algorithms used on the biomedical engineering.

1.2 OBJECTIVES

In order to achieve the overall objective of developing software and hardware solutions for biomedical engineering applications, in particular, array signal processing techniques, we present the following specific objectives:

- **OE1**: Propose a MWHD, including high-resolution signal processing algorithms to measure of the HR and the steps;
- **OE2**: Propose a modification of the traditional eigenvalue based ITC, such that it can estimate the amount of components of MEG and EEG data;
- **OE3**: Propose an unsupervised framework for the identification of VEP in MEG measurements;
- **OE4**: Validate our results using measurements.

1.3 CONTRIBUTIONS OF THIS WORK

The main contribution of this work is the proposal of solutions in the biomedical area. However, along the PhD research, additional contributions on the area of cybersecurity were also published. Next, the papers published in journals in the reverse chronological order during the PhD research are listed.

- [4] Pinheiro, G. P. M.; Miranda, R. K.; Praciano, B. J. G.; Santos, G. A.; Mendonça, F. L. L.; Javidi, E.; da Costa, J. P. C. L.; de Sousa Jr., R. T. *Multi-Sensor Wearable Health Device Framework for Real-Time Monitoring of Elderly Patients Using a Mobile Application and High-Resolution Parameter Estimation*. Frontiers in Human Neuroscience, 2022
- [5] Maranhão, J. P. A.; da Costa, J. P. C. L.; de Freitas, E. P.; Javidi, E.; de Sousa Jr., R. T. *Error-Robust Distributed Denial of Service Attack Detection Based on an Average Common Feature Extraction Technique*. Sensors, v. 20, p. 5845, 2020
- [6] Maranhão, J. P. A.; da Costa, J. P. C. L.; de Freitas, E. P.; Javidi, E.; de Sousa Jr., R. T. *Noise-Robust Multilayer Perceptron Architecture for Distributed Denial of Service Attack Detection*. IEEE Commuications Letters, v. 1, p. 1-1, 2020
- [7] Maranhão, J. P. A.; da Costa, J. P. C. L.; de Freitas, E. P.; Javidi, E.; Borges, C. A.; de Sousa Jr., R. T. *Tensor based framework for Distributed Denial of Service attack detection*. Journal of Network and Computer Applications, v. 1, p. 102894, 2020

Next, the conference papers published during the PhD research are listed in the reverse chronological order.

- [8] Maranhão, J. P. A.; da Costa, J. P. C. L. ; Javidi, E. ; Sousa Jr., R. T. ; Milanezi Jr., J. *Multidimensional Antenna Array based Framework for Drone Localization in Multipath Environments*. In: International Conference on Signal Processing and Communication Systems (ICSPCS), 2019, Gold Coast.

- [9] Javidi, E.; da Costa, J. P. C. L.; Miranda, R. K.; Maranhão, J. P. A.; Vargas, J. A. R. *Modified Information Theoretic Criteria for Low Complexity Estimation of the Amount of Components in MEG Measurements*. In: International Conference on Signal Processing and Communication Systems (ICSPCS), 2019, Gold Coast

- [10] Javidi, E.; da Costa, J. P. C. L.; Miranda, R. K.; Maranhão, J. P. A.; Vargas, J. A. R. *Unsupervised Framework for the Identification of Visual Evoked Potential in MEG Measurements*. In: International Conference on Signal Processing and Communication Systems (ICSPCS), 2019, Gold Coast

- [11] Rega, D. G. ; Miranda, R. K.; Javidi, E.; Maranhão, J. P. A.; da Costa, J. P. C. L.; Pinheiro, G. P. M. *ESPRIT-Based Step Count for Wearable Devices*. In: International Conference on Signal Processing and Communication Systems (ICSPCS), 2019, Gold Coast

1.4 OVERALL ORGANIZATION

In addition to this introduction, this PhD thesis contains three more chapters and four appendices, as described below. Chapter 2 presents a complete framework for health systems composed of a MWHD, high-resolution parameter estimations, and a real-time monitoring application. Chapter 3 proposes an unsupervised framework for the identification of VEP in MEG measurements, including a solution for the *Model Order Selection* (MOS). In Chapter 4, the conclusions are drawn and future research topics are provided. The contents of Chapters 2 are published in [4], and Chapter 3 is covered in [9] and [10].

Appendix A summarizes the cybersecurity contributions in [7], while Appendix B has the signal processing algorithms of the MWHD [4] used in Chapter 2, Appendix C outlines the application of the algorithms of the Appendix B on the step counter [11] and Appendix D overviews the application of the *Multiple Denoising* (MuDe) algorithm for drone localization [8].

2 MULTI-SENSOR WEARABLE HEALTH DEVICE FRAMEWORK

Automatized scalable healthcare solutions allow real-time 24/7 health monitoring of patients, prioritizing medical treatment according to their health conditions, reducing medical appointments in clinics and hospitals, and easy exchange of information between the medical body. State-of-the-art health wearable device platforms present limitations in hardware, parameter estimation algorithms, and software architecture. This chapter proposes a complete framework for health systems composed of a multi-sensor wearable health device (MWHD), high-resolution parameter estimations, and a real-time monitoring application. The hardware includes sensors for monitoring steps, pulse oximetry, heart rate (HR), and temperature, with data transmission using low-power wireless communication. In terms of parameter estimation, the embedded circuit processes high-resolution signal processing algorithms, allowing an improved measure of the HR and the steps. The proposed high-resolution signal processing-based approach outperforms state-of-the-art HR estimation measurements using measurements of the photoplethysmography (PPG) sensor.

2.1 INTRODUCTION

Nowadays, health systems, including hospitals and their *Intensive Care Units* (ICU), are challenged by a substantial need to increase critical care capacity due to the Coronavirus Disease 2019 (COVID-19) pandemic [12]. The importance of streamlining workflows for rapid diagnosis and isolation, clinical management, and infection prevention essential to caring for COVID-19 patients, to protect healthcare workers and other patients while supporting ICU practitioners' activities, hospital administrators, governments, and policymakers is highlighted in [12].

As suggested in [13], health systems invest in automatized and scalable digital health solutions, such as healthcare wearable devices empowered with artificial intelligence information systems. Automatized digital health solutions allow real-time 24/7 health monitoring of patients, prioritizing medical treatment according to the patients' health conditions, reducing medical appointments in clinics and hospitals, and securing information between the medical body.

According to [14], the global market for wearable medical devices was valued at USD 13 billion in 2019, with an expected annual growth rate of 27.9% until 2027. Still, according

to [14], multi-sensor health wearable devices are becoming popular due to the cost reduction of remote health monitoring technologies, including home healthcare.

In this chapter, we propose a MWHD framework with real-time monitoring application and high-resolution parameter estimation. The proposed hardware includes sensors for step counting, pulse oximetry, HR, and temperature measurements. Since wireless communications require a significant consumption of device battery energy [15, 16], the proposed MWHD optimizes the battery usage by using *Bluetooth Low Energy* (BLE). In terms of parameter estimation, the embedded integrated circuit programmed with high-resolution signal processing algorithms processes the sensors' signals, allowing improved analysis of the steps, pulse oximetry, and HR. Finally, the patient's medical information is reliably provided to healthcare workers by the real-time monitoring application.

This chapter is composed of five sections, including this introduction as Section 2.1. In Section 2.2, related works in health data signal processing and healthcare platforms are shown. In Section 2.3.1, we propose a wearable device prototype using PPG, an algorithm for HR estimation, and a software platform architecture for remote healthcare supervision. Section 2.4 presents the methodology and results of the performance comparison of PPG processing algorithms for HR estimation. Section 2.5 concludes the chapter.

2.2 STATE OF THE ART

In [17], the feasibility of a compact wearable sensor patch for measurements of different physiological signals, including PPG and body temperature, is presented. The wearable sensor system transmits the physiological measurements wirelessly to a gateway using a BLE module. The health data is encrypted, stored, and analyzed on the Internet cloud.

In [18], a digital filter for PPG signals collected from an MWHD is proposed using an adaptive neural network, allowing a more accurate estimate of the HR, resulting in a variation of 3% concerning the ground truth. In [19], a deep learning approach is proposed for the HR estimation using PPG signals, achieving an absolute error of 1.5 BPM, outperforming state-of-the-art methods. The authors of [20] present a new deep learning model with the capability to estimate HR using only a single channel provided by the PPG signal, achieving an error for HR estimation of 0.046 BPM. Note that the usage of neural networks requires labeled data and the tuning of the neural network hyperparameters.

In [21], a new ring-shaped sensor is proposed to estimate the heartbeat using reflective PPG. The measurements are transmitted to a mobile phone via Bluetooth 4.0. In comparison with the commercial solution, the ring-shaped sensor presented an error of 2% smaller.

In [22], it improves the HR estimation by using a new notch filter, and the noise cancella-

tion approach is based on the least mean squares. The error of the HR estimation employing this approach is smaller than 1 BPM using measurements from intensive physical activities.

Reference [23] discusses challenges in HR estimation from a wrist band with PPG collected during intense exercises. First, *Principal Component Analysis* (PCA) and adaptive filtering are used for removing noise from the PPG signals. Then, to estimate the HR, a *Support Vector Machine* (SVM) based approach is considered. The approach in [23] presents errors of 1.01 BPM.

A novel health wearable platform for the real-time monitoring of accidents of elderly people is shown in [24]. In terms of performance, the improved sensors in [24] present a longer battery lifetime, allowing their usage by elderly people during long periods.

In [25], a new method is proposed to estimate HR using PPG. The method also includes BSS to improve the results further. The achieved RMSE is 6.1 BPM.

2.2.1 State-of-the-art simplified model for PPG waveforms

The PPG waveform can be modeled as a pulsating quasi-periodic component attributed to synchronous cardiac changes in the blood volume with each heartbeat. This pulsating component is superimposed by a slowly varying low-frequency component, with various lower frequency components attributed to respiration, sympathetic nervous system activity, and thermoregulation [26]. The PPG signal is sampled with a sampling rate of f_s. Such sampled PPG waveform is modeled by:

$$x[n] = A\cos\left[2\pi f n + \theta\right] + r[n], \tag{2.1}$$

where A is the PPG signal amplitude, f is the relative frequency of the PPG signal normalized by f_s, θ is the phase of the PPG signal, and $r[n]$ is a component that comprises the noise and artifacts present in the PPG signal. Note that, due to the *Heart Rate Variability* (HRV) [27] and the *Inter-Beat Intervals* (IBI), HR is a time variable. However, we assume a short estimation interval, such that the model in (2.1) can be applied.

HR detection can then be formulated as a frequency estimation problem. Thus, by measuring the frequency parameter f of a periodic heart signal, given in Hz, we convert the HR to the corresponding value in BPM, given by $\text{BPM} = f \cdot 60$.

In the literature, common approaches for the HR estimation that are applied in embedded systems include *Fast-Fourier Transform* (FFT) based [28], autocorrelation [29], zero-crossing detection [30] and peak detection [31]. These approaches are summarized in Appendix B.

2.3 PROPOSED HEALTHCARE PLATFORM COMPOSED OF LOW-COST HARDWARE, HIGH-RESOLUTION PARAMETER ESTIMATION ALGORITHMS AND REAL-TIME MONITORING APPLICATION ARCHITECTURE

This section, as depicted in Figure 2.1, proposes the multi-sensor health wearable device framework with real-time monitoring application and high-resolution parameter estimation. According to Figure 2.1, each patient is assigned an MWHD, which gathers and processes each subject's health data. The MWHD then transmits the processed data via a wireless communication protocol based on BLE to a concentrator device. Note that the concentrator hardware depicted in Figure 2.1 has been proposed in [32]. This concentrator device uploads data to a cloud server, which interacts with the proposed monitoring application installed on healthcare workers' mobile devices. The healthcare workers are thus able to monitor patients and collaborate in real-time.

This section is divided into three subsections. In Subsection 2.3.1, we detail the proposed MWHD. In Subsection 2.3.2, we propose the high-resolution processing algorithm for HR estimation. In Subsection 2.3.3, we propose the healthcare platform for real-time monitoring.

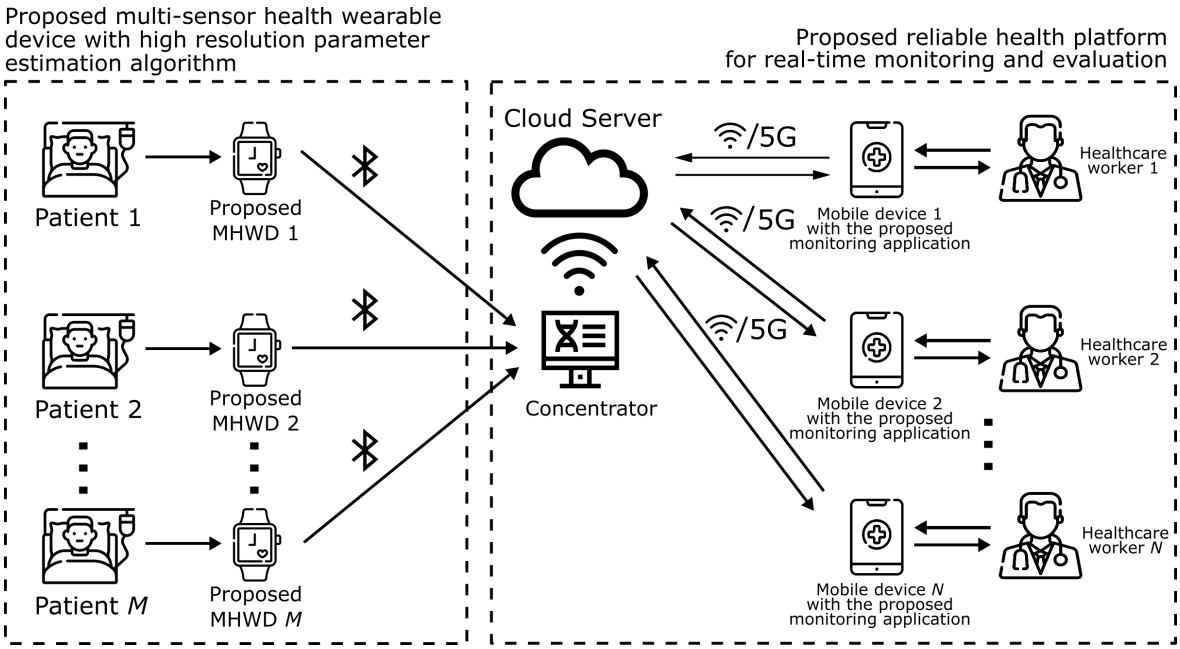

Figure 2.1 – Diagram of the proposed healthcare framework, consisting of a multi-sensor health wearable device, PPG high resolution parameter estimation and real-time monitoring application.

2.3.1 Proposed healthcare wearable device including multiple sensors, processor and low energy wireless communication

The proposed MWHD prototype showed in Figure 2.2 is battery-operated and contains sensors to measure health information of the user – namely HR, pulse oximetry, body temperature, and steps. The sensors communicate over an *Inter-Integrated Circuit* (I^2C) bus with the *Microcontroller Unit* (MCU). The MCU then transmits data to mobile devices using BLE, thus minimizing power consumption.

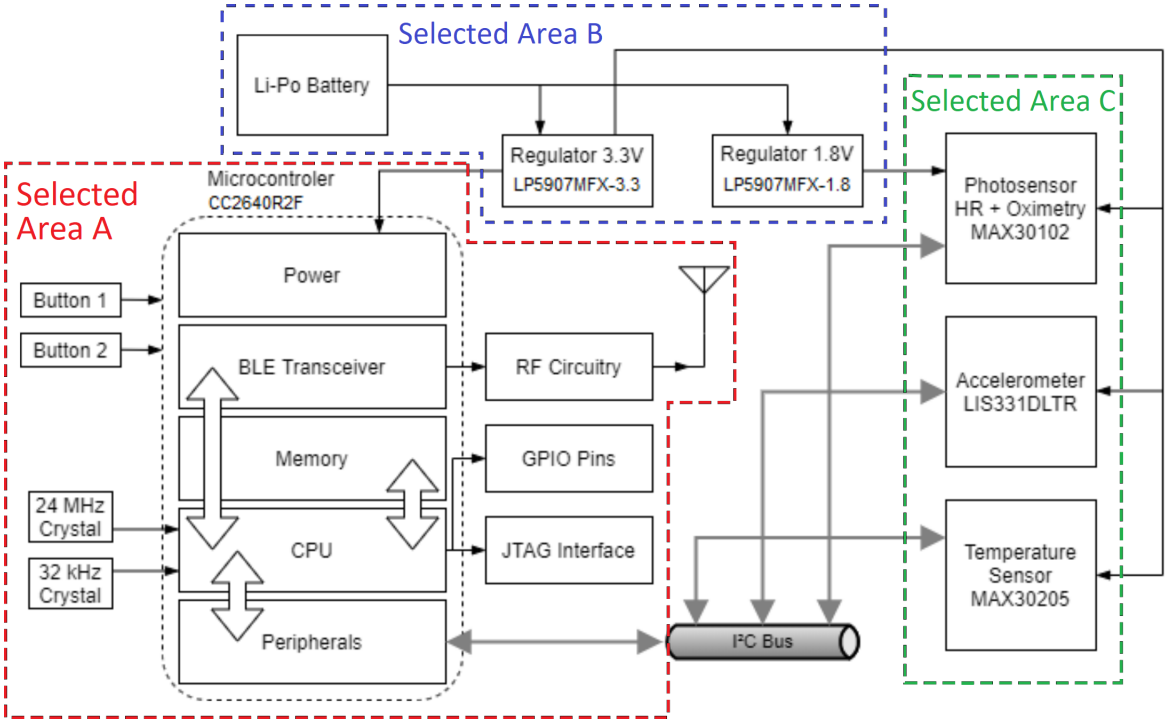

Figure 2.2 – Block diagram showing the functional circuit components of the proposed prototype wristband.

Selected Area A of Figure 2.2 comprises the CC2640R2F Cortex®-M3 MCU circuit [33] and additional components for operating the MCU and for the BLE communication interface. Two crystals are positioned to generate clock signals for different modes of the MCU, one with 24 MHz for regular speed operation and 32 kHz for low-power mode. The reduced speed during low-power mode saves power during idle operation. The *General Purpose Input/Output* (GPIO) pins and *Joint Test Action Group* (JTAG) Interface are made available in pin connectors for ease of access during testing of the MWHD prototype. The *Radiofrequency* (RF) circuitry is built according to the recommendations on [33] related to the 4 x 4 External Single-ended configuration, which requires a smaller board space and saves more power. Two push-buttons are added for user input and interaction with the device.

Selected Area B of Figure 2.2 is the power sourcing part of the circuit from a small *Lithium-Polymer* (LiPo) battery. The nominal 3.7 V of the LiPo battery is regulated to 3.3 V and 1.8 V using low-dropout regulators LP5907MFX-3.3 and LP5907MFX-1.8. The regula-

tors guarantee a stable voltage of operation for the MCU and sensors during device operation and battery's charge and discharge cycles. The LiPo battery is equipped with a generic commercial micro USB recharging module with overcharge, over-discharge, and current protections.

Selected Area C of Figure 2.2 includes the sensors for health data measurements. The signals provided by the PPG sensor MAX30102 are used to estimate the HR and pulse oxymetry using red or *Infrared* (IR) LEDs. Red and IR LED signals in conjunction enable pulse oximetry estimation, based on the different absorption rates of arterial and venous blood. The prototype device also comprises an accelerometer LIS331DLTR, used for the step counter, to measure movement artifacts used for interference reduction on the PPG signal. For keeping track of body temperature variations, such as fever, the prototype utilizes a MAX30205 sensor. The sensor is positioned on the bottom side of the prototype device to contact the users' skin. The values read are calibrated according to the manufacturer's specifications in [34].

The proposed *Printed Circuit Board* (PCB) is designed as a 4-layer board to achieve routing requirements and reduce *Electromagnetic Interference* (EMI). Additionally, the proposed PCB is double-sided mounted, with central processor and input buttons on the top and sensors on the bottom to contact the user's wrist skin (required by PPG and body temperature measurements). Test points are also positioned for power sourcing, communication interfaces, and JTAG debugging.

Figure 2.3 shows photos of the MWHD prototype produced according to the block diagram of Figure 2.2. On the left-hand side photo, the complete prototype encapsulated as a smartband is shown, while on the right-hand side photo, the PCB of the block diagram of Figure 2.2 is depicted.

The MWHD is projected as a low-cost device, enabling a cheaper complete healthcare solution to be deployed on a large scale. The cost of the components and PCB was USD 25.00 in a low volume run, indicating that further cost reduction is possible by bulk production. The final price of the device is on-par with other low-cost fitness wearable devices available in the market. This cost compares well with those of clinical health devices, that can cost more than USD 100.00, by a considerable margin.

As we carried out the hardware prototype development and the proposed algorithm for HR estimation simultaneously, we gathered HR data from a MAX30100 device for experimental validation. This different PPG sensor module is equivalent to that present in the projected prototype. The employed pulse oximeter and HR sensor integrated circuit captured data in peripheral oxygen saturation (SPO_2) measuring mode, though pulse oximetry data is not presently considered. Data from the IR LED from the sensor is considered during the tests due to reduced interference from ambient background lighting, while the red LED

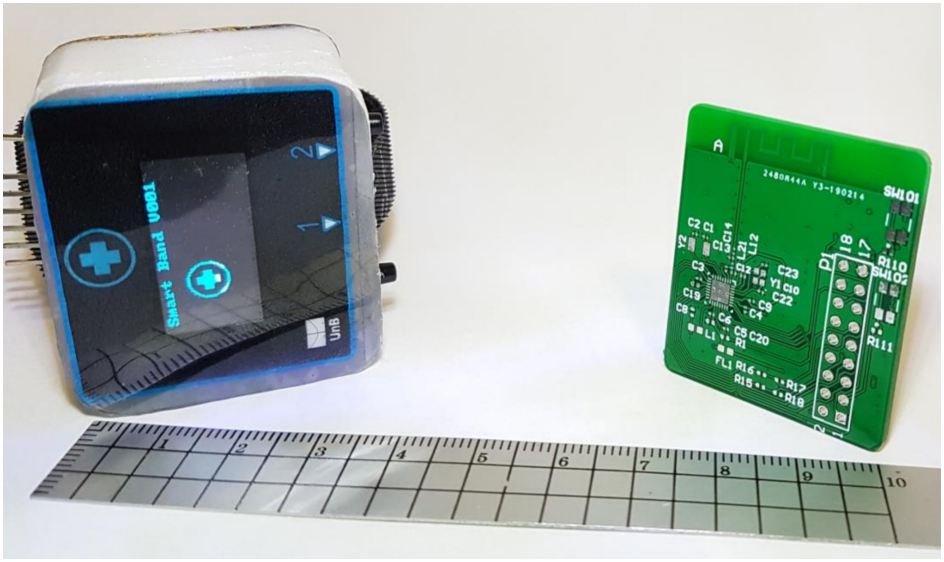

Figure 2.3 – Dimensions of the PCB and enclosure produced for the proposed MWHD device prototype.

data is disregarded for the application.

The MAX30100 PPG sensor module communicates via I^2C bus to the main MCU, which then transmits gathered data to the computer's serial port via a USB-to-Serial adapter. The experiment uses wired serial transmission.

2.3.2 Proposed high resolution signal processing algorithm for HR estimation

A novel approach for HR detection applying the *Estimation of Signal Parameters by Rotational Invariance Techniques* (ESPRIT) [35] algorithm is presented in this subsection. In [36], the high-resolution signal processing technique named SPHINS is successfully applied for the frequency estimation in forensic applications. In [37], a high accuracy step counter algorithm based on ESPRIT has been proposed using the accelerometer signals acquired by the sensors of our MWHD prototype proposed in Subsection 2.3.1. Inspired by the outstanding results of [36, 37, 38], we propose the usage of the high-resolution signal processing algorithm ESPRIT to measure the HR.

The algorithm exploits the property of rotational invariance of signal subspaces spanned by two temporally displaced data sets [35]. A simplified description of the least-squared version of the ESPRIT algorithm is shown next based on [38] and [39].

By applying the Hilbert transform on the PPG waveform model in (2.1), we obtain the analytic representation of the signal $x[n] \in \mathbb{R}$ given by:

$$y[n] = x[n] + j\mathcal{H}\{x[n]\}, \tag{2.2}$$

where the operator $\mathcal{H}\{\}$ denotes the *Discrete Hilbert Transform* (DHT) and $j = \sqrt{-1}$.

We replace (2.1) into (2.2) and rewrite $y[n] \in \mathbb{C}$ by taking into account that $\mathcal{H}\{\}$ is a linear operator, as:

$$y[n] = A\cos\left[2\pi fn + \theta\right] + j\mathcal{H}\{A\cos\left[2\pi fn + \theta\right]\} + r[n] + j\mathcal{H}\{r[n]\}. \tag{2.3}$$

The signal $y[n]$ can then be represented as a sum of the complex exponentials with added noise component $w[n]$, comprising the real and imaginary parts of the noise component $r[n]$:

$$y[n] = A\exp j[2\pi fn + \theta] + w[n]. \tag{2.4}$$

By segmenting the samples obtained by $y[n]$ in (2.4), we can build a data matrix $\mathbf{Y}$ where N is the amount of data records of the length-P time-window vector signal $y[n]$, thus:

$$\mathbf{Y} = [\mathbf{y}[0] \quad \mathbf{y}[1] \quad \dots \quad \mathbf{y}[N-1]]^{\mathrm{T}} \quad \in \quad \mathbb{C}^{P\times N}, \tag{2.5}$$

where $\mathbf{y}[n] = [\widehat{y}[n]\ \widehat{y}[n+1]\ \dots\ \widehat{y}[n+P-1]]^{\mathrm{T}}$, and $^{\mathrm{T}}$ is the transposition operator of matrices.

Next we compute the sample covariance matrix of (2.5) as follows:

$$\mathbf{R}_y = \frac{\mathbf{Y}\mathbf{Y}^{\mathrm{H}}}{N}. \tag{2.6}$$

By applying the *Eigenvalue Decomposition* (EVD) in (2.6), we obtain the following expression:

$$\mathbf{R}_y = \mathbf{U}\mathbf{\Sigma}\mathbf{U}^{\mathrm{H}}, \tag{2.7}$$

where $\mathbf{U}$ is an $P \times P$ matrix of right singular vectors and $^{\mathrm{H}}$ denotes the Hermitian operator. Matrix $\mathbf{\Sigma} \in \mathbb{R}^{N\times P}$ has dimensions $N \times P$ and is composed of singular values.

Matrix $\mathbf{U}$ can be decomposed as $\mathbf{U} = [\mathbf{u}_{y_0}|\mathbf{U}_{\mathrm{w}}]$, where $\mathbf{u}_{y_0}$, the first column of $\mathbf{U}$, is the vector that generates the signal subspace, of dimensions $P \times 1$, formed by the singular vector corresponding to the maximum singular value of the data matrix $\mathbf{Y}$. The remaining singular vectors form a matrix in which its columns correspond to the basis that generate the noise subspace $\mathbf{U}_{\mathrm{w}}$, of dimensions $P \times (P-1)$, orthogonal to the signal subspace.

By writing vectors $\mathbf{u}_u$ and $\mathbf{u}_d$ formed by the first and last $P-1$ elements of $\mathbf{u}_{y_0}$, respectively, the rotational invariance presented previously, and exploited by ESPRIT, guarantees that:

$$\mathbf{u}_u\phi = \mathbf{u}_d, \tag{2.8}$$

where $\phi \in \mathbb{C}$ corresponds to the rotation scalar. By solving (2.8), the phase value estimation

of ϕ is given by:

$$\phi = \angle \frac{\mathbf{u}_u^{\mathrm{H}} \mathbf{u}_d}{\mathbf{u}_u^{\mathrm{H}} \mathbf{u}_u}, \tag{2.9}$$

where $\angle$ is the phase notation that denotes the phase angle value of the corresponding complex number.

We determine the frequency estimator $\widehat{f}$ with the computed phase angle value of ϕ and the sampling frequency f_s, thus:

$$\widehat{f} = \frac{\phi}{2\pi} \cdot f_s. \tag{2.10}$$

To estimate HR, we calculate the time window T of the measurement given by $T = n_{\text{samples}}/f_s$, that is equivalent to the duration of the measurement in seconds. Finally, the estimated value is BPM $= \widehat{f} \cdot 60/T$.

Next, we present the summarized steps of the ESPRIT based algorithm for the HR estimation.

Algorithm 1: Proposed ESPRIT-based HR estimation via Hilbert Transform

1 Given signal $x[n]$ in (2.1), sampled with frequency f_s, during a time window of T:
2 1) Obtain signal $y[n]$ according to (2.3) by applying the Discrete Hilbert Transform to $x[n]$.
3 2) Segment the samples obtained in signal $y[n]$ to obtain the data matrix $\mathbf{Y}$ in (2.5)
4 3) Compute the sample covariance matrix estimate $\mathbf{R_y}$ of the data matrix $\mathbf{Y}$ as in (2.6).
5 4) Decompose $\mathbf{R_y}$ in the corresponding EVD matrices to calculate by eigendecomposition matrix $\mathbf{U}$ according to (2.7), whose columns are the corresponding right eigenvectors of $\mathbf{R_y}$.
6 5) Determine the column $\mathbf{u}_{y_0}$ of matrix $\mathbf{U}$, corresponding to the maximum singular value of data matrix $\mathbf{Y}$.
7 6) Determine $\mathbf{u}_u$ and $\mathbf{u}_d$ by taking the first and last $P-1$ elements of vector $\mathbf{u}_{y_0}$.
8 7) Estimate the rotation scalar $\phi \in \mathbb{C}$ from vectors $\mathbf{u}_u$ and $\mathbf{u}_d$ based on the rotational invariance property as in (2.8).
9 8) Extract the estimated angle value of ϕ from (2.9).
10 9) Determine the frequency estimator using phase angle value of ϕ into (2.10).
11 10) Calculate the estimated BPM value equal to $\widehat{f} \cdot 60/T$.

2.3.3 Healthcare platform for real-time monitoring and evaluation

The software architecture of the proposed application is divided into five layers, as depicted in Figure 2.4.

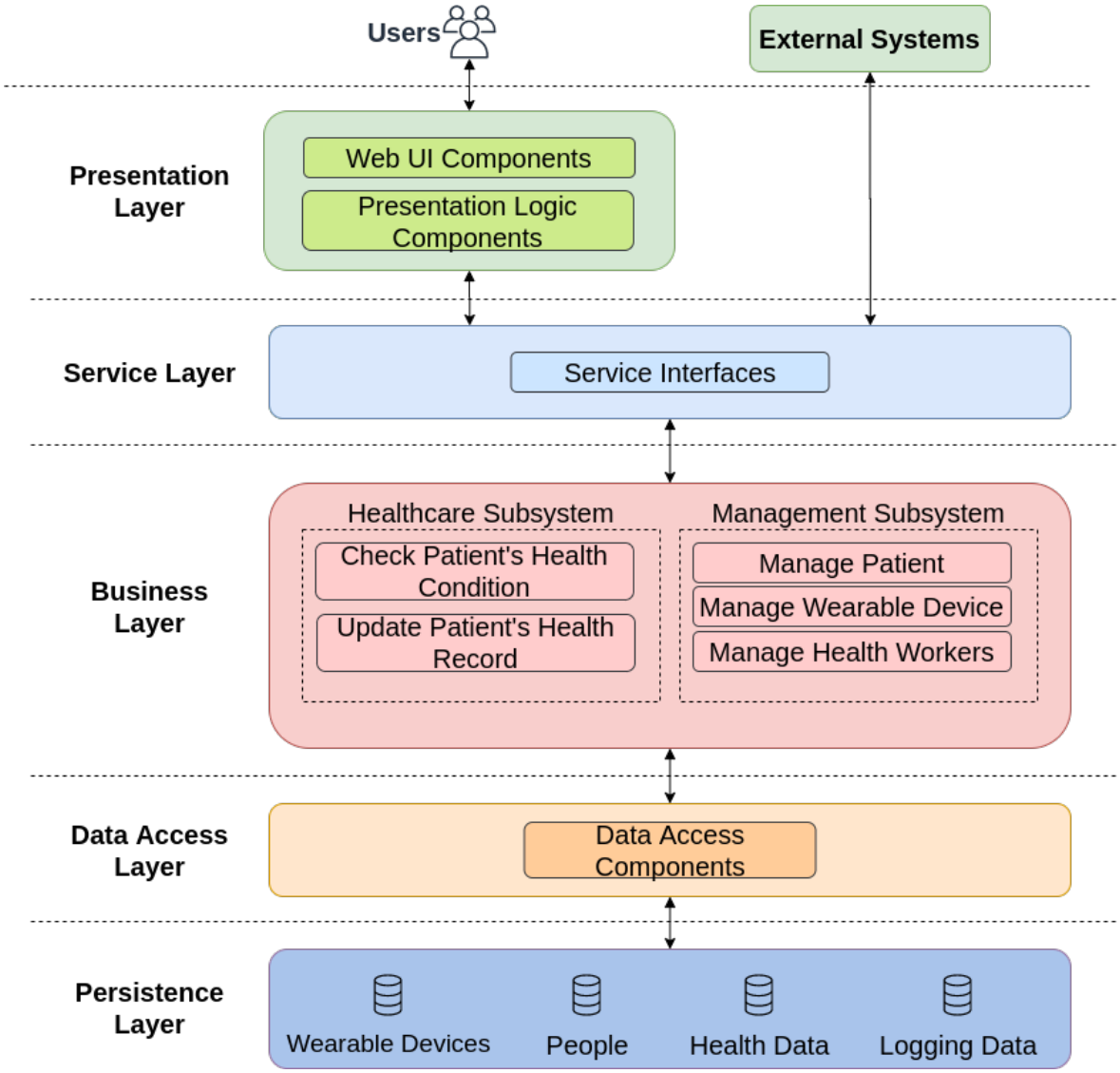

Figure 2.4 – Software architecture for the developed real-time monitoring healthcare application.

In the Presentation Layer of Figure 2.4, a login screen for authentication and registration of new users is defined. This feature allows users to register and identify their medical credentials and securely store their information in the application servers.

The Service Layer of Figure 2.4 exposes the business logic implemented in the software to potential consumers. One example of an external system is the concentrator responsible for uploading data from wearable devices.

The Business Layer of Figure 2.4 is the logic behind the platform. We divided this layer into two blocks, in which the Healthcare Subsystem is used to check the data generated from the patient, and the other block, called Management Subsystem, provides administrative functions, such as supervise and manage multiple patients, wearables, and healthcare workers.

The Data Access Layer of Figure 2.4 contains components to abstract the logic required to access the data stores. Such components provide common data access functionality, isolating the upper layers from the specific database technology, and making the application easier to maintain and configure.

The Persistence Layer of Figure 2.4 provides several advantages to the software since it is more efficient to save, retrieve and provide data for the whole application. In our context, we have four data sources, namely: Wearable Devices, People, Health Data, and Logging Data.

One advantage of the proposed online application in the solution framework is its interaction with the end-user. Using the platform, healthcare workers can track multiple users' health conditions in a centralized and reliable manner. Note that the proposed real-time monitoring platform can be integrated into other MWHD, as exemplified in [32], with the usage of a commercial MWHD.

Although the subject of security is not a focus of this chapter, it is essential to highlight that a distributed system such as the proposed healthcare application, which involves interactions following the paradigm and includes personal data and requires fully distributed security measures [40]. This is particularly crucial for lightweight protocols for the authentication of devices, as proposed in [41].

2.4 EXPERIMENTAL VALIDATION

To evaluate the performance of the proposed ESPRIT-based HR estimation approach in Subsection 2.3.2, measurements using the PPG sensor equivalent to that of Subsection 2.3.1 are considered. The MAX30100 sensor used for this experimental validation [42] has an ADC with lower resolution than that available in the MAX30102 [43] sensor present in the MWHD prototype, and also different possible parameter configurations. We believe the results presented here are extensible to the proposed MWHD due to equivalences in both sensors' PPG technology.

Initially, signal pre-processing is performed on the sampled data to eliminate artifacts and other detrimental factors that would hinder each HR estimator's performance. Such processes are employed to account for signal processing present in PPG systems' real operation, maintaining this work's scope.

Motion artifacts are removed using an outlier detector that removes abruptly varying artifacts from the signal based on the derivative's high absolute values between consecutive samples. A low-frequency blocker filter — as proposed in [44] — is implemented with $R = 0.95$ to filter most of the low frequency noise in the signal. A 6-th order Butterworth

low-pass filter with a cutoff frequency of 4 Hz is applied to attenuate high-frequency noise. It leaves an effective bandwidth that can detect an HR of up to 240 BPM.

To establish a referential target value for the real HR value, two commercial MWHD were simultaneously used as the experiment was carried out. The first is a medical oximeter ELERA SH-K3 that measures HR and pulse oximetry using red and infrared light for transmissive PPG, worn on the user's finger. The second device is a fitness smartband Fitbit Charge HR that comprises two green light LEDs for reflective PPG, worn on the user's wrist. Immediately before and after each measurement, HR values of both devices were logged. It gives initial and final reference values for each device in the measurement time frame, allowing for HR variation during the experiment to be taken into account. The values measured after the experiment are then used as true values for calculating the RMSE of each estimator. We believe that the sensors' final readings better reflect the BPM values during the experiment, as they include the same time window of the sample measurements.

The pre-processed samples are used as input for the algorithms under text, resulting in estimations of the true HR value. Results are expressed in terms of the RMSE, given by:

$$\text{RMSE}(f, \widehat{f}) = \sqrt{\frac{1}{n_{\text{samples}}} \sum_{i=0}^{n_{\text{samples}}-1} (f_i - \widehat{f}_i)^2}, \tag{2.11}$$

calculated for each estimator $\widehat{f}_i$, referenced either from the oximeter or smartband true value f_i as read at the end of each measurement.

For experimental validation, PPG sensor configurations are varied to evaluate each algorithm's capabilities and robustness. Initially, the IR LED current level, which controls its transmission power, is investigated using the values made available on the sensor. Lower IR current levels decrease the device energy consumption. However, as the LED power also decreases, the detected signal is weaker, which may increase the estimation error. Configurations above 30.6 A saturated the sensor's ADC, implying into no meaningful data. The remaining measurements were processed with a signal time window of 5 seconds and a sample rate of 100 Hz, amounting to 500 samples. In Figure 2.5, results are presented considering the oximeter reference, while Figure 2.6 refers to the smartband values read right after experimental measurements ended.

According to Figures 2.5 and 2.6, the proposed algorithm based on ESPRIT resulted in lower RMSE values for most of the current values considered. Moreover, the proposed algorithm could perform more accurately at lower current levels, indicating it can save more power. Note that the zero crossing approach completely fails, since it is not robust enough to process the data. Lack of robustness of the zero crossing approach is caused by the usage of single sample, while the other approaches combine the samples to perform the estimation.

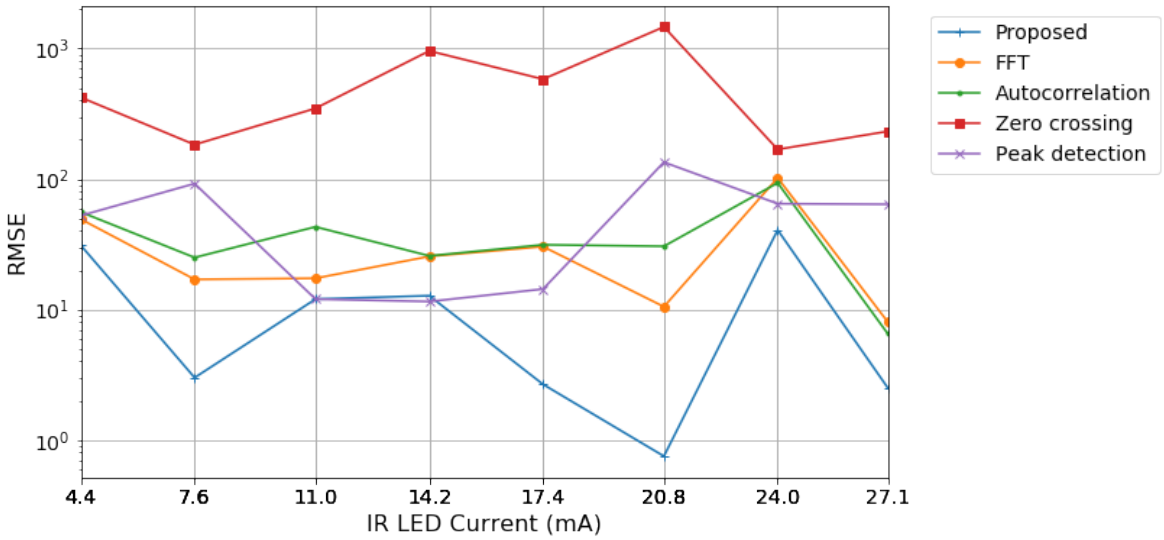

Figure 2.5 – RMSE of estimated BPM values for each algorithm for different current level configurations, referenced to values read by the oximeter.

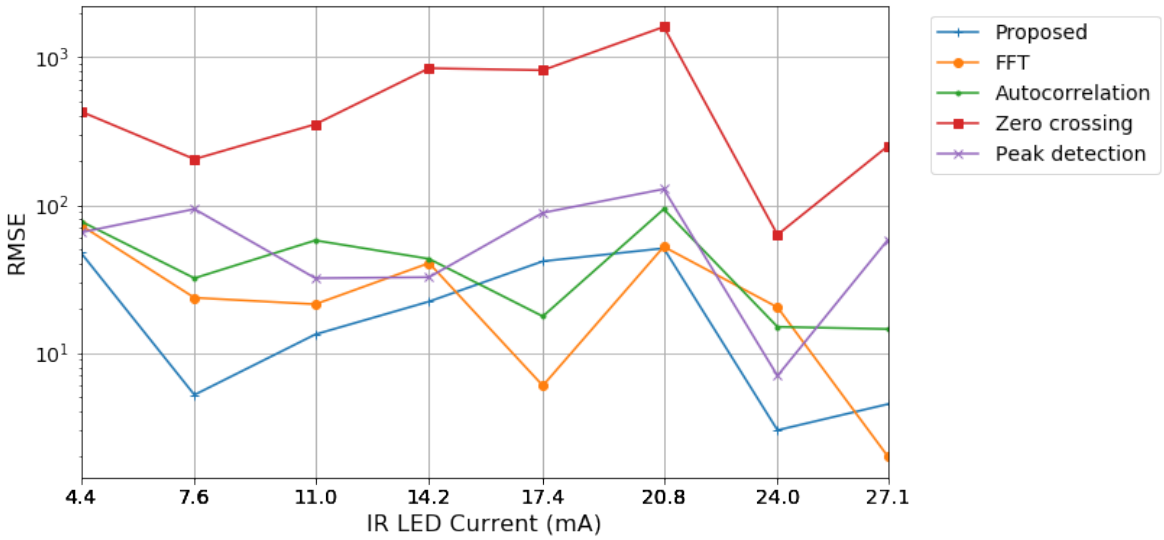

Figure 2.6 – RMSE of estimated BPM values for each algorithm for different current level configurations, referenced to values read by the smartband.

In Figures 2.7 and 2.8, we varied the IR LED pulse width. Longer pulse widths increase power consumption and the detected signal's length, enabling the ADC to settle in a more precise value. Consequently, the ADC resolution available at the sensor is dependent on the selected pulse width, whose possible values are shown in Table 2.1. Experimental data was gathered, fixing the LED current level at 27.1 mA and sample rate at 100 Hz. Data were processed with 500 samples, corresponding to a 5 seconds time window. The RMSE of the estimations is presented by the final readings of each reference considered. Figure 2.7 corresponds to the oximeter, while Figure 2.8 corresponds to the smartband.

Table 2.1 – LED pulse width configurations tested and the correspondent ADC resolution.

Pulse width (μs)	**ADC Resolution (bits)**
1600	16
800	15
400	14
200	13

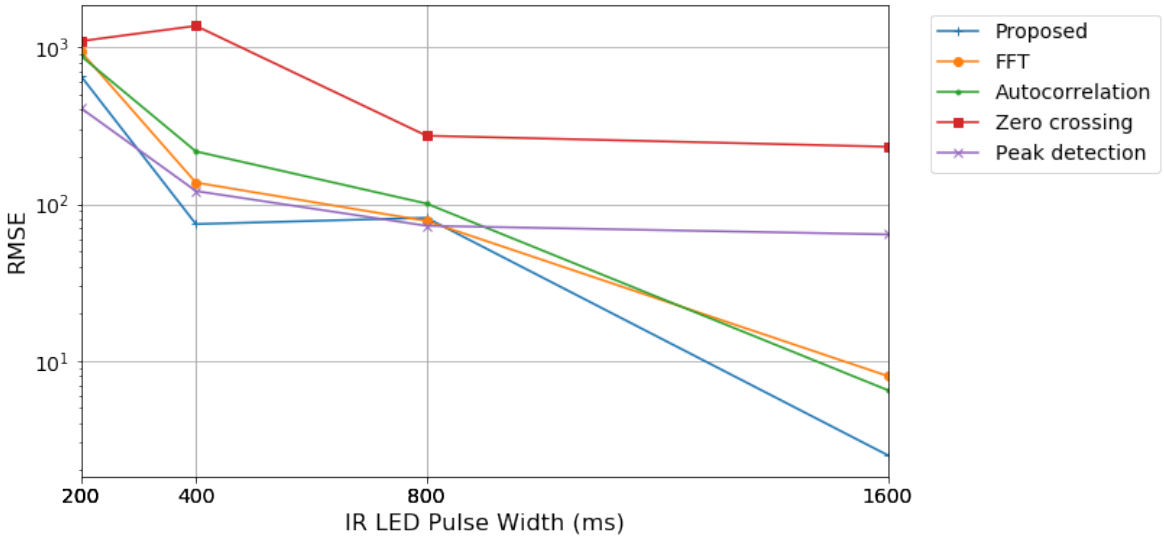

Figure 2.7 – RMSE of estimated BPM values for different pulse width and corresponding ADC resolution configurations, referenced to values read by the oximeter.

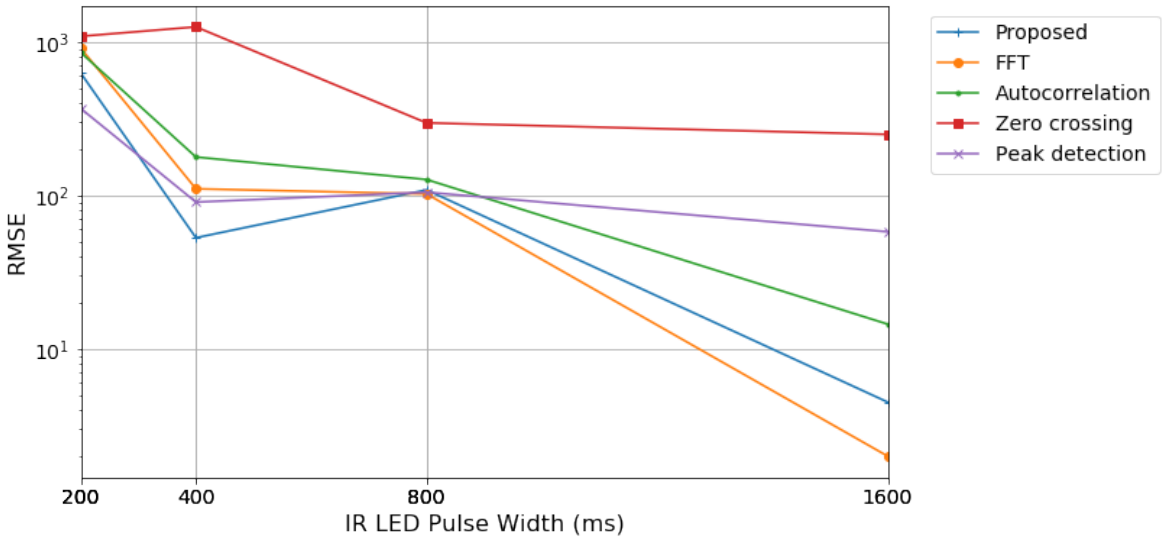

Figure 2.8 – RMSE of estimated BPM values for each algorithm for different pulse width and corresponding ADC resolution configurations, referenced to values read by the smartband.

The estimator results are consistent with the previous test case, with the proposed algorithm generally having lower RMSE values. These tests showed significant results regarding

algorithm performance with reduced pulse width and ADC resolution. Pulse width shorter than 50% of the maximum value is shown to degrade estimation precision considerably. The shortest pulse width generated higher error values than other configurations. This may be due to signal ripple caused in *Pulse-Width Modulation* (PWM) operation, which is more substantial the shorter the pulse is. Another factor to take into consideration is the lower ADC resolution corresponding to lower LED pulse width. Therefore, along with suspected ripple noise, a lower sampling resolution can further impair the output PPG parameter estimation.

We also validate variations in the sample rate to corroborate with the previous experimental stages. The experimental results obtained show that higher sample rates have decreased precision in HR, possibly due to the imposed reduction in ADC resolution in each configuration tested, as can be seen in Table 2.2. Hence, a sample rate of 100 Hz is considered advantageous, since it maintains a larger signal bandwidth and maximum ADC resolution.

Table 2.2 – Maximum available ADC resolution for each sample rate configuration tested.

Sample rate (Hz)	**ADC Resolution (bits)**
50	16
100	16
167	15
200	15
400	14

The proposed algorithm based on ESPRIT showed consistent results throughout the experiments performed. It generally has lower RMSE values for lower IR LED current configurations and lower sampling frequencies, following the general trend in the pulse width variation. Hence, besides the increased precision, it demonstrates the potential for power-saving and more resilient performance in challenging scenarios.

An analysis of power consumption of the proposed MWHD was carried out in [45] and is summarized here for further experimental validation. The current consumption was measured as 2.032 mA on average. That leads to a total battery autonomy of the MWHD of approximately 73 hours, about a small-sized 150 mAh LiPo battery. Moreover, that enables the MWHD to be used for around three days without recharging, adding comfort to patients' use.

The connection between the MWHD and the real-time monitoring application is possible due to the *Representational State Transfer* (REST) protocol. Based on this protocol, we built an API to perform this connection with the database. We computed the times in different requests for the different pages of the platform. The results are presented in Table 2.3.

Table 2.3 – Access times to different test requests performed to the API of the real-time monitoring application.

Action	Access Time (ms)
Retrieve data from feed page	43.87
Access patient's profile	95.0
Add new patient	97.70
List teams	61.19
Request patients list	213.08
Add new healthcare worker	36.01

As shown in Table 2.3, the low latency of access validates that the proposed online platform can be used for real-time monitoring.

2.5 SUMMARY OF THE CHAPTER

This chapter proposes a multi-sensor wearable health device framework and a real-time monitoring application with high-resolution parameter estimation. The proposed hardware includes sensors for step counting, pulse oximetry, HR, and temperature. The proposed MWHD optimizes battery usage by using BLE. In terms of parameter estimation, the embedded system programmed with high-resolution algorithms processes signals from the multiple sensors used, allowing an improved estimation of the steps and HR. Finally, the patient's medical information is reliably provided to the healthcare workers by the real-time monitoring application.

3 IDENTIFICATION OF VISUAL EVOKED POTENTIAL IN MEASUREMENTS

VEP plays a crucial role in the diagnosis of nerve diseases and epilepsy. By applying luminous stimulation in different frequencies, neuronal electrical voltage changes are measured in the visual cortex area at the rear of the head using MEG. Such acquired MEG signals are separated into components using BSS. The MEG measurements are analyzed by medical experts and, based on their subjective interpretation, the VEP components are identified. Supervised Machine Learning (ML) methods can be applied to identify VEP components. However, these methods require labeled data, which must be generated through the subjective interpretation of medical experts. This can be limiting as medical experts traditionally assume a fixed amount of components. This chapter proposes a blind framework to estimate the model order of the MEG measurements and to extract the VEP components. In order to estimate the amount of components, the framework exploits a low computational complexity modified AIC and does not require human intervention. In order to overcome the need for labeled data, we propose three approaches to automatically compare components extracted from MEG measurements with and without stimulation. Since each proposed unsupervised identification approach identifies a set of VEP components, we propose their decision fusion using set operations. The proposed framework does not require any human intervention, and it can be used as a complementary tool to support experts in identifying VEP components. The results are presented in terms of average amplitude spectrum and spectral topography. The proposed framework is validated using real MEG measurements.

3.1 INTRODUCTION

MEG is a non-invasive neurophysiological method in which the magnetic activity of the brain is measured based on the voltage fluctuations on the skull surface. Evoked potentials correspond to changes in the electrical activity of neuronal structures of the nervous system that occur as a result of targeted external stimulation of a sensory organ or peripheral nerve. Evoked potentials are used to study the conductivity of neural pathways by neurological methods. In particular, Visual Evoked Potential VEP is a certain form of evoked potential that allows assessment of the optic nerve and visual pathway [46, 47].

Due to the visual stimulation of the retina, triggered electrical voltage changes in the

visual cortex at the back of the head can be measured as VEP. MEG derives the VEP over the primary visual cortex, which allows for diagnosing optic nerve diseases. One crucial step in the VEP analysis from MEG measurements is selecting the number of components before applying a BSS scheme [48], such as the *Independent Component Analysis* (ICA) .

While traditionally, the estimation of the number of components relies on the subjective visual assessment by experts [49, 50, 51], alternative approaches have been proposed in the literature. One such approach is ICASSO [52], which is designed specifically for this purpose. However, ICASSO has limitations with respect to its extensive computational complexity and the need for human intervention to establish appropriate thresholds for identifying resolvable components. Furthermore, conventional eigenvalue-based ITC, such as AIC [53, 54] and MDL [54], do not possess the capability to estimate the number of components from MEG measurements directly [10, 55].

In this context, a fully automatic framework is proposed to determine the model order selection and to identify VEP components. In contrast to traditional supervised machine learning approaches, which depend on training data, the proposed unsupervised framework relies on the independent components obtained from measurements with and without stimulation to enable the estimation of VEP components.

The main contributions of this chapter are:

- Proposal of the automatic framework for estimation of the amount of components and identification of the VEP components by exploiting parts of our contributions in [10], [55], and [9];
- Proposal of three variations of approaches to compare the components extracted from the measurements in order to identify the VEP components;
- In order to use the three approaches without human supervision, we propose a calibration approach exploiting the correlation levels of the MEG measurements with and without stimulation;
- Finally, we validate the results using flashes with different frequencies.

The rest of this chapter is organized as follows. In Section 3.2, the proposed framework for VEP identification is overviewed using a block diagram with all steps. In Section 3.3, we show the state of the art for the estimation of the amount of components. In Section 3.4, we show our proposed modified ITC components- As shown in 3.5, the modified AIC outperforms the other modified ITC approaches. Therefore, we summarize the steps of the modified AIC in Section 3.6. In Section 3.7, we propose three automatic approaches for the unsupervised framework to identify the VEP components. In Section 3.8, the experiments

results including their analysis are presented. Finally, a chapter summary is presented in Section 3.9.

3.2 OVERVIEW OF THE PROPOSED FRAMEWORK FOR VEP IDENTIFICATION

This section presents the proposed unsupervised framework to determine the VEP components from the MEG measurements. In this section, we give an overview of the proposed unsupervised framework. The incorporation of low complexity modified AIC into the framework is shown in Section 3.6. In Section 3.7, three proposed unsupervised identification approaches and their respective calibrations are shown. In Subsection 3.7.3, two approaches to subjective VEP identification by visual inspection are presented, the first applying average amplitude spectrum and spectral topography, and the second processing the data applying resolution and overlap parameters. Finally, in Subsection 3.7.4, the proposed approach for merging the outputs of the previous modules is detailed.

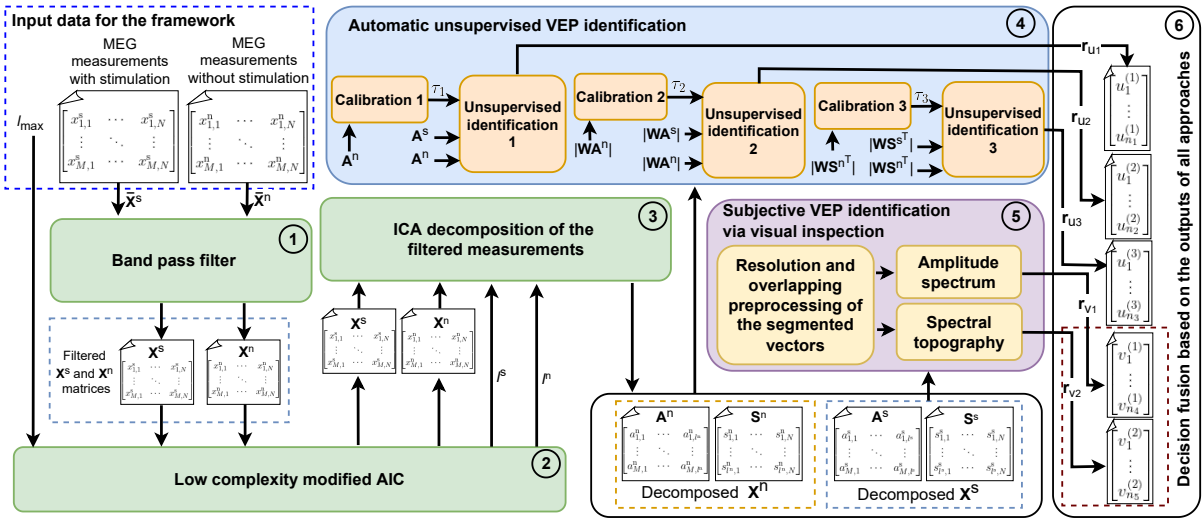

Figure 3.1 – Proposed framework for model order selection and unsupervised identification of visually evoked potential components

According to Figure 3.1, the inputs of **Step 1** are the variable $I_{\max}$, which is an upper limit for the number of components, and two matrices, $\mathbf{X}^{\mathrm{s}}$ and $\mathbf{X}^{\mathrm{n}}$, which were obtained from measurements where M channels of the MEG magnetometer were used. The device used is the Elekta Neurogam depicted in Fig. 3.2. Note that the device has mesaurements from MEG, EEG and EOG. However, the scopus of this chapter is the analisys of the MEG measurements.

The matrix $\mathbf{X}^{\mathrm{s}}$ comprises the moments with stimulation blocks, and the matrix $\mathbf{X}^{\mathrm{n}}$ represents the interval without stimulation between stimulation blocks. Note that each row of

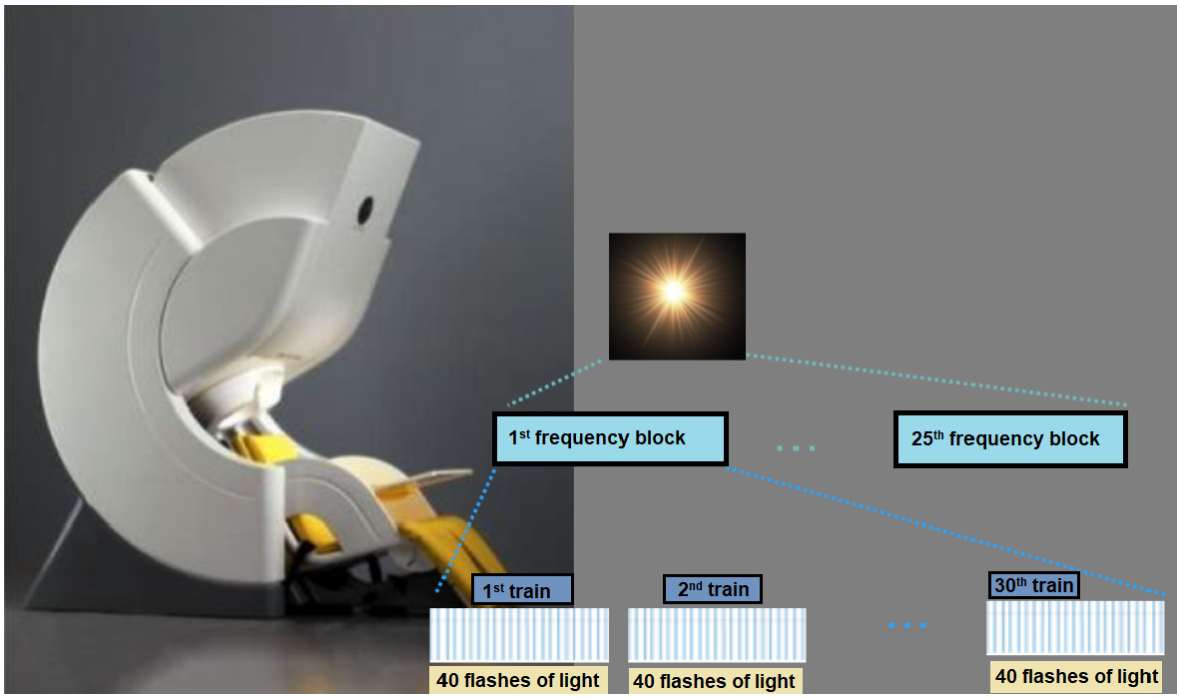

Figure 3.2 – Measurement device Elekta Neuromag with flicker stimulation in the Biomagnetic Center at the Jena University Hospital

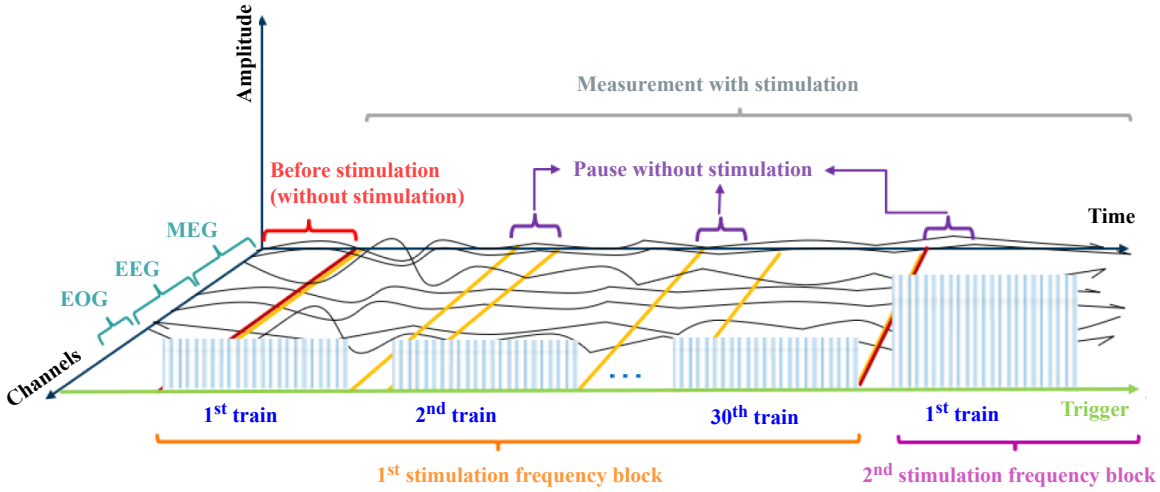

Figure 3.3 – Data Structure

the matrix $\mathbf{X}^s$ has size $N_z \cdot N_w \cdot P$, where P is the amount of samples in each period of the flash, N_w is the amount of flashes in a train, and N_z is the amount of trains.

In **Step 1** of Figure 3.1, a high-pass filter with a cut-off frequency of f_{high} and a low-pass filter with a cut-off frequency of f_{low} are used. Moreover, a notch filter of f_{notch} is applied to remove the interference of the electric grid. These filters are applied to both stimulated and unstimulated measurement data.

In **Step 2** of Figure 3.1, we present the proposed low complexity modified AIC, which, according to our contribution in [9, 55], provides a performance similar to ICASSO, but

with a much lower computational complexity. Note that other low-complexity modified ITC schemes, such as modified Minimum Description Length (MDL), modified Efficient Detection Criterion (EDC), and modified Bayesian Information Criterion (BIC), are outperformed by the modified AIC. The outputs of **Step 2** are the estimated model orders I^{s} and I^{n} of the measurements with and without stimulation, respectively.

In **Step 3** of Figure 3.1, ICA is employed to decompose the matrices $\mathbf{X}^{\mathrm{s}}$ and $\mathbf{X}^{\mathrm{n}}$ into the sum of I^{s} independent components.

In **Step 4** of Figure 3.1, VEPs are identified by exploiting the mixing matrices A^{s} and A^{n} and the source matrices S^{s} and S^{n}. In this proposal, three different approaches are introduced for identifying VEP components, allowing the results of each approach to be evaluated. According to Subsection III-C, three different approaches are used to identify VEP independent components from the I^{s} independent components with stimulation using different calibration parameters τ for each approach. Still in Subsection III-C, we propose in **Step 4** of Figure 1 a calibration approach in order to find a suitable value of τ by using the independent components without stimulation.

In **Step 5** of Figure 3.1, each row of each independent component is transformed into a new matrix by concatenating the segments according to two parameters, namely resolution r and overlap l. Additional details regarding the parameters r and l can be found in Subsection 3.7.3. In **Step 5** of Figure 3.1, it is important to note that only the matrices A^{s} and S^{s} are utilized as input.

In **Step 6** of Figure 3.1, we propose a decision fusion approach of the VEP independent components by applying the set operation to the VEP components obtained from the approaches in **Step 4** and **Step 5**. Note that each of the five approaches already provides a set of VEP components that can be directly used.

3.3 STATE-OF-THE-ART APPROCHES FOR THE ESTIMATION OF THE AMOUNT OF COMPONENTS

The estimation of the amount of components is a crucial step necessary for any BSS scheme, such as FastICA. Therefore, in this section, we present the state-of-the-art approaches for the estimation of the amount of components. In Subsection 3.3.1, an overview of ICASSO is provided, while, in Subsection 3.3.2, an overview of eigenvalue-based ITC is presented.

3.3.1 Estimation of the amount of components by visual inspection via ICASSO

ICASSO is a FastICA based approach that exploits the fact that if the amount of components is correctly estimated, then the different realizations of the FastICA may result into very well distinguished clusters [52]. In general, the following instantaneous mixture data model is assumed for the derivation of BSS schemes.

$$\boldsymbol{X}_0 = \sum_{i=1}^{I_\mathrm{e}} \boldsymbol{X}_i^{(\mathrm{e})} = \sum_{i=1}^{I_\mathrm{e}} \boldsymbol{a}_i^{(\mathrm{e})} \boldsymbol{s}_i^{(\mathrm{e})} = \boldsymbol{A}^{(\mathrm{e})} \boldsymbol{S}^{(\mathrm{e})}, \tag{3.1}$$

where $\boldsymbol{X}_0 \in \mathbb{R}^{M \times N}$ is the measured data $\boldsymbol{X}^s$ without noise and $\boldsymbol{X}_i^{(\mathrm{e})}$ are denoted as the I_e well distinguished components or resolvable components or specular components. The mixture matrix $\boldsymbol{A}^{(\mathrm{e})} \in \mathbb{R}^{M \times I_e}$ includes the vectors $\boldsymbol{a}_i^{(\mathrm{e})}$ for $i = 1, \ldots, I_\mathrm{e}$. The source signal matrix $\boldsymbol{S}^{(\mathrm{e})} \in \mathbb{R}^{I_e \times N}$ is composed of the source vectors for each group of neurons $\boldsymbol{s}_i^{(\mathrm{e})} \in \mathbb{R}^{1 \times N}$ for $i = 1, \ldots, L_\mathrm{e}$.

A more complete model in comparison with (3.1) is given as follows

$$\boldsymbol{X} = \sum_{i=1}^{I_\mathrm{e}} \boldsymbol{X}_i^{(\mathrm{e})} + \sum_{i=1}^{I_\mathrm{d}} \boldsymbol{X}_i^{(\mathrm{d})} + \boldsymbol{N}, \tag{3.2}$$

where $\boldsymbol{X} \in \mathbb{R}^{M \times N}$ is the magnetometer channel matrix, $\boldsymbol{X}_i^{(\mathrm{e})}$ is the i-th specular component, $\boldsymbol{X}_i^{(\mathrm{d})}$ is the i-th dense component and $\boldsymbol{N}$ is the noise. Note that I_e and I_d are the amount of specular components and the amount of dense components, respectively [50].

In order to apply the ICASSO to estimate the amount of components, it is crucial to provide a maximum amount of components denoted by I_{max}. By increasing too much I_{max}, the computational complexity and necessary memory of ICASSO becomes even more prohibitive. However, a small number of I_{max} may result into $I_{\mathrm{max}} < I_e$ implying into a high risk of not finding the VEP component. The more realizations of FastICA are performed, the better is the ICASSO performance. The authors in [52] recommend approximately 25 realizations at least for a good accuracy for ICASSO. However, in this case, the computational burden of ICASSO is extremely high, if the amount of sensors and snapshots of the measured data are large.

By applying ICASSO, the estimation of the amount of both specular and dense components is feasible. In order to exemplify, we consider Figure 3.4. Figure 3.4 depicts the similarity plot obtained by applying ICASSO in our measurements considering volunteer 1 and the stimulation frequency at 3.84 Hz. Note that there are clusters that are very well separated from the other ones. These clusters are named the specular components. There are also clusters with overlaps and we refer to them as dense components. According to [52], the estimation of the amount of components should be performed taking into account both

specular and dense components. Therefore, in Figure 3.4, we can estimate that $I_e + 1 = 9$ components, while $I_e + I_d = 26$ components. Still according to [52], we should apply a BSS considering the amount of components as $I_e + I_d = 26$. By using the amount of components equal to $I_e + I_d$ in the ICA decomposition, the ICA returns components that are not interpretable. Therefore, the goal is to find an amount of components that is at least between $I_e + 1$ and $I_e + I_d$ such that we guarantee that the VEP component is present, when the BSS scheme is applied. By using $I_e + 1$ as the amount of components, we may be able to decompose the measured matrix into I_e specular components and one dense component. On the other hand, by using $I_e + I_d$ as the amount of components, we may be able to decompose the measured matrix into I_e specular components and I_d dense components. Note that, if the estimated amount of components is even greater than $I_e + I_d$, the BSS approach requires an unnecessary increased computational complexity due to the increased amount of components. Moreover, noise components can be mistakenly selected as the VEP component.

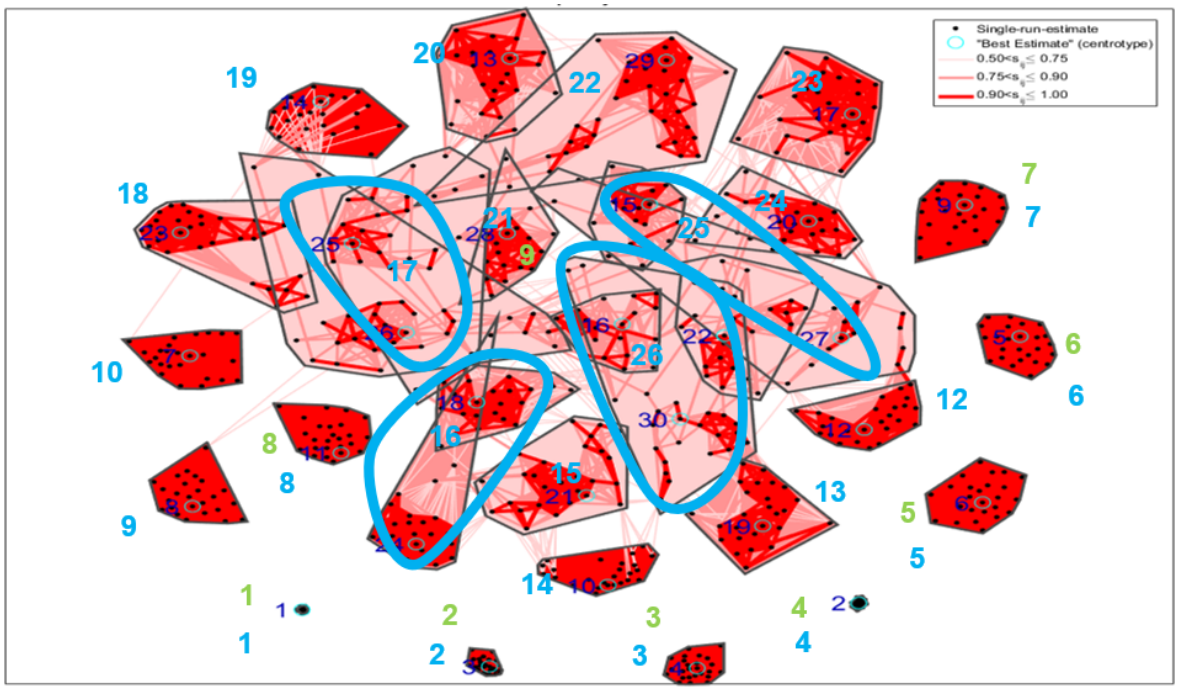

Figure 3.4 – Estimation of the amount of components using ICASSO similarity plot of block frequency at $f_{s_1} = 3.84$ Hz of the first volunteer.

3.3.2 Estimation of the amount of components via ITC

In contrast to the ICASSO, that can estimate the components as shown in Subsection III-A, the eigenvalue-based ITC is not suitable to estimate L_e and L_d from the preprocessed measured data matrix $\boldsymbol{X}$ modeled in (3.2). Therefore, by applying it in MEG measurements, it completely fails in the estimation of $L_e + L_d$ or L_e.

The eigenvalue-based ITC schemes rely on the eigenvalues profile of the sample covari-

ance matrix of $\boldsymbol{X}$. The sample covariance matrix is computed as

$$\widehat{\boldsymbol{R}}_{xx} = \frac{\boldsymbol{X}^s \boldsymbol{X}^{s\mathrm{T}}}{N} \in \mathbb{R}^{M \times M}. \tag{3.3}$$

By applying the Eigenvalue decomposition of (3.3), $\widehat{\boldsymbol{R}}_{xx}$ can be written as

$$\widehat{\boldsymbol{R}}_{xx} = \boldsymbol{E}\boldsymbol{\Sigma}\boldsymbol{E}^{\mathrm{T}}, \tag{3.4}$$

where $\boldsymbol{E} \in \mathbb{R}^{M \times M}$ is the eigenvector matrix and $\boldsymbol{\Sigma} \in \mathbb{R}^{M \times M}$ is the eigenvalue matrix. By applying the operator $\mathrm{diag}(\cdot)$ on $\boldsymbol{\Sigma}$, we can extract the vector of the main diagonal only with the eigenvalues.

By applying $\mathrm{diag}(\boldsymbol{\Sigma})$ on the expression in (3.5), we obtain an estimate of the amount of components. Note that (3.6) is sum of two terms. The left term is derived as a function of the maximum log-likelihood function exploiting the eigenvalue decomposition, while the right term is denoted as the penalty function and maps the amount of the degrees of freedom. By varying k from 0 to $M-1$, the value of k that minimizes $J(k)$ is the estimated of components as follows

$$\widehat{L} = \underset{k}{\operatorname{argmin}}\, J(k), \tag{3.5}$$

$$J(k) = -N(M-k)\log\left(\frac{g(k)}{a(k)}\right) + p(k, N, M), \tag{3.6}$$

where $\widehat{L}$ is the estimated amount of components, k is the candidate value for the amount of components, $g(k)$ is the geometric mean of the k smallest eigenvalues and $a(k)$ is the arithmetic mean of the k smallest eigenvalues.

In general each ITC has a specific penalty function $p(k, N, M)$. For instance, for the AIC, the penalty function is given by

$$p(k, N, M) = k(2M - k), \tag{3.7}$$

Another ITC is the MDL [54] and its penalty function is given by

$$p(k, N, M) = \frac{1}{2}k(2M - k)\log(N), \tag{3.8}$$

Depending on the scenario, for instance, data contaminated with colored noise, the EDC [56] may result into improved results. Its penalty function is given by

$$p(k, N, M) = \frac{1}{2}k(2M - k)\sqrt{N \ln N}, \tag{3.9}$$

Finally, the BIC penalty function is given by

$$p(k, N, M) = 2k(2M - k)\log(N), \tag{3.10}$$

3.4 PROPOSED MODIFIED APPROACHES FOR THE ESTIMATION OF THE AMOUNT OF COMPONENTS

Although the ITC schemes in Subsection 3.3.2 have a very low computational complexity in comparison with ICASSO, they are not suitable to estimate I_e and I_d from the MEG data according to the model in (3.2).

As shown in Subsection 3.3.1, ICASSO requires information about the maximum value of the amount of components I_{max} to work with a non-prohibitive complexity and memory allocation. In Subsection 3.4.1, we modify the ITC schemes by exploiting the information of I_{max}. We propose two different approaches. The first approach is based on the estimation of the amount of components exploiting the sample covariance matrix from the estimated channel matrix using I_{max}. In Subsection 3.4.2, a second approach very similar to the approach in Subsection 3.3.2 is proposed by replacing M and N by I_{max}.

3.4.1 Estimation of the amount of components combining FastICA with ITC

Inspired by the ICASSO, that is based on multiple realizations of the FastICA, we propose a scheme based on only one FastICA realization and on the traditional ITC.

By applying the FastICA, we can decompose the data as follows

$$\boldsymbol{X} \approx \widehat{\boldsymbol{A}}\widehat{\boldsymbol{S}} = \sum_{i=1}^{I_{\mathrm{max}}} \widehat{\boldsymbol{a}}_i \widehat{\boldsymbol{s}}_i, \tag{3.11}$$

where $\widehat{\boldsymbol{A}} \in \mathbb{R}^{M \times I_{\mathrm{max}}}$ is the estimated mixing matrix and $\widehat{\boldsymbol{S}} \in \mathbb{R}^{I_{\mathrm{max}} \times N}$ is the estimated source matrix.

By computing the sample covariance matrix of the estimated source matrix, we obtain

$$\widehat{\boldsymbol{R}}_{SS} = \frac{\boldsymbol{S}\boldsymbol{S}^{\mathrm{T}}}{N} = \sigma_{\mathrm{s}}^2 \boldsymbol{I} \quad \in \mathbb{R}^{I_{\mathrm{max}} \times I_{\mathrm{max}}}, \tag{3.12}$$

where σ_{s}^2 is the variance of the source signal and $\boldsymbol{I}$ is the unitary matrix. Due to the FastICA,

the vectors $\widehat{s}_i$, for $i = 1, ..., I_{max}$, are orthogonal to each other.

Given that $\widehat{\boldsymbol{R}}_{XX}$ from (3.3) is a full matrix, i.e. not diagonal, and given that $\widehat{\boldsymbol{R}}_{SS}$ is diagonal, then the sample covariance matrix $\widehat{\boldsymbol{R}}_{AA}$ is full and is given by

$$\widehat{\boldsymbol{R}}_{AA} = \frac{\boldsymbol{A}\boldsymbol{A}^{\mathrm{T}}}{L_{max}} \in \mathbb{R}^{M \times M}. \tag{3.13}$$

Note that since $M > I_{\mathrm{max}}$, then $\widehat{\boldsymbol{R}}_{AA}$ has rank I_{max}. Therefore, only the I_{max} greatest eigenvalues of $\widehat{\boldsymbol{R}}_{AA}$ are different from zero and the remaing $M - I_{\mathrm{max}}$ smallest eigenvalues are equal to zero.

By applying the eigenvalue decomposition, $\widehat{\boldsymbol{R}}_{AA}$ can be represented as

$$\widehat{\boldsymbol{R}}_{AA} = \boldsymbol{E}_{AA}\boldsymbol{\Sigma}_{AA}\boldsymbol{E}_{AA}^{\mathrm{T}}, \tag{3.14}$$

where $\boldsymbol{E}_{AA}$ is the eigenvalue matrix and $\boldsymbol{\Sigma}_{AA}$ is the eigenvector matrix. The vectors with the eigenvectors are represented by diag($\boldsymbol{\Sigma}_{AA}$) and are used for the estimation of the amount of components.

Note that the parameters $M \times N$ of (3.6) are function of the size of $\widehat{\boldsymbol{X}} \in \mathbb{R}^{M \times N}$. Therefore, we can modify (3.6) to the size of $\widehat{\boldsymbol{A}} \in \mathbb{R}^{M \times I_{\mathrm{max}}}$. Hence, we can rewrite (3.6) in the following fashion

$$J(k) = -I_{\mathrm{max}}(I_{\mathrm{max}} - k)\log\left(\frac{g(k)}{a(k)}\right) + p(k, I_{\mathrm{max}}, I_{\mathrm{max}}), \tag{3.15}$$

where $g(k)$ and $a(k)$ are the geometric and the arithmetic mean of the k smallest elements of the following vector diag($\boldsymbol{\Sigma}_{AA}$)$(1 : I_{max})$. Note that diag($\boldsymbol{\Sigma}_{AA}$)$(1 : I_{\mathrm{max}})$ has the non-zero eigenvalues of $\widehat{\boldsymbol{A}}$.

Comparing (3.6) and (3.15), we note that M is replaced by I_{max}, since M is the maximum value of the amount of components. Moreover, N is replaced by I_{max}, since the total amount of samples of $\widehat{\boldsymbol{A}}$ is given by I_{max}.

3.4.2 Estimation of components of the sample covariance matrix using the modified ITC approaches

Inspired by the approach proposed in Subsection 3.4.1, we can select the I_{max} greatest eigenvalues of diag($\boldsymbol{\Sigma}$)$(1 : I_{\mathrm{max}})$ from (3.4). In this case, we apply diag($\boldsymbol{\Sigma}$)$(1 : I_{\mathrm{max}})$ directly into (3.15).

3.5 EXPERIMENTAL RESULTS

In this section, we compare the performance of the state-of-the-art approaches in Section 3.3 with the proposed modified scheme in Section 3.4 in terms of accuracy and time processing. In Subsection 3.5.1, we compare the schemes in terms of accuracy considering the ICASSO as a reference due to the visual inspection, while, in Subsection 3.5.2, we compare the schemes in terms of time processing. For the results of this section, we have selected the measurements of the first volunteer and only two block frequencies: 3.84 Hz and 21.73 Hz.

3.5.1 Comparing schemes in terms of estimation of the amount of components

By applying the ICASSO according to Subsection 3.3.1, we obtain the results in Table 3.1. Note that $\widehat{I}_d > \widehat{I}_e$ in both scenarios and note that $\widehat{L}_e$ is greater than the traditional values used the literature [57, 50, 51] , such as 1 to 5 components.

Table 3.1 – Estimated amount of components of measurements with and without stimulation of the first volunteer.

	$\widehat{I}_e + 1$	$\widehat{I}_e + \widehat{I}_d$
$f_{s_1} = 3.84$	9	26
$f_{s_2} = 21.73$ Hz	9	22

Next we evaluate the performance of the traditional ITC schemes in Subsection 3.3.2. As shown in Figure 3.5, the eigenvalues profile does not follow the assumptions used in their derivation. One major assumption is the flat profile for the noise eigenvalues. In total there are 102 eigenvalues. Therefore, note that the 64 greatest eigenvalues are much higher than the 38 smallest eigenvalues. The values of the 38 smallest eigenvalues range around 10^{-8}, while the 64 greatest eigenvalues are greater than one. This break in eigenvalue profile degrades the estimation of $I_e + 1$ and $I_e + I_d$ performed by the state-of-the-art ITC reviewed in Subsection 3.3.2.

As shown in Tables 3.2 and 3.3, by using all 102 eigenvalues of diag($\mathbf{\Sigma}_{xx}$), all ITC fails indicating an amount of components equal to 64.

In Figure 3.6, we compute the $L_{\max}$ eigenvalues of the sample covariance matrix $\widehat{\boldsymbol{R}}_{AA}$ for the block frequency 3.84 Hz using the modified expression in (3.15) proposed in Subsection 3.4.1. Note that the estimates of AIC and MDL equal to 23 and 14, respectively, in Table 3.2 are in the range of ICASSO between $\widehat{I}_e + 1 = 9$ and $\widehat{I}_e + \widehat{I}_d = 26$ in Table 3.1. In this case, both techniques are suitable. If the goal is to reduce the computational complexity, the MDL is more suitable due to its underestimation. If the goal is to estimate more components considering the case that the VEP may be too weak, then the overestimation of AIC is more

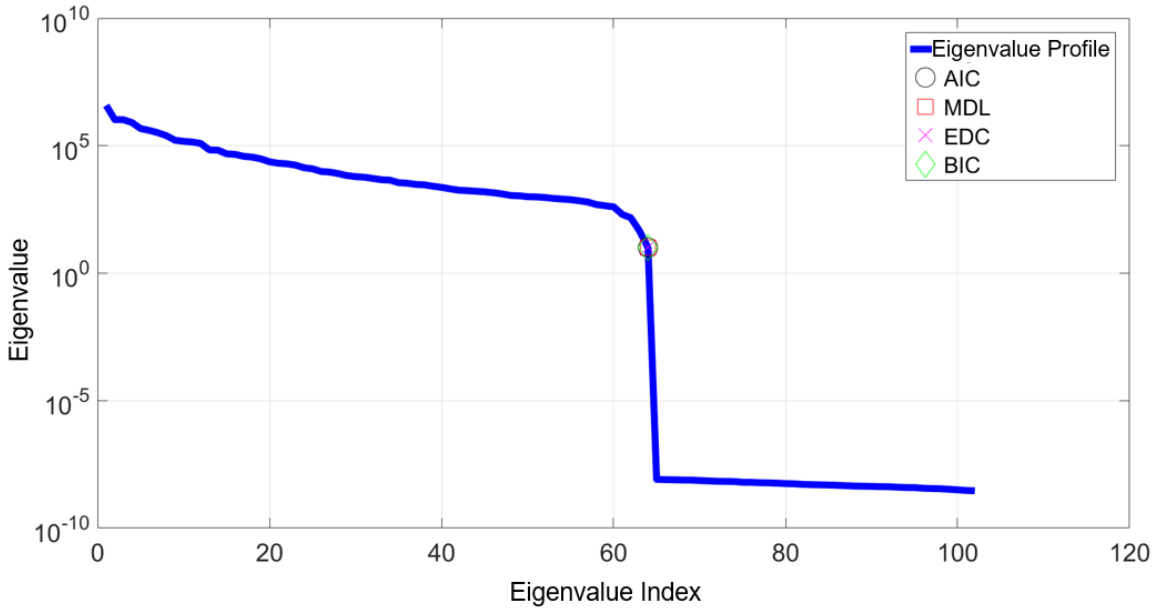

Figure 3.5 – Estimation amount of components using the state-of-the-art ITC shown in Subsection 3.3.2 using the main diagonal of the matrix $(\mathbf{\Sigma}_X)$ of the measurements of block frequency at 3.84 Hz of the first volunteer.

suitable.

As shown in Table 3.3, even with the modified expression in (3.15) proposed in Subsection 3.4.1, the EDC and BIC still fail in the estimation of the amount of components, since their estimated values 4 and 1, respectively, are much smaller than $\widehat{I}_e + 1 = 9$ in Table 3.1.

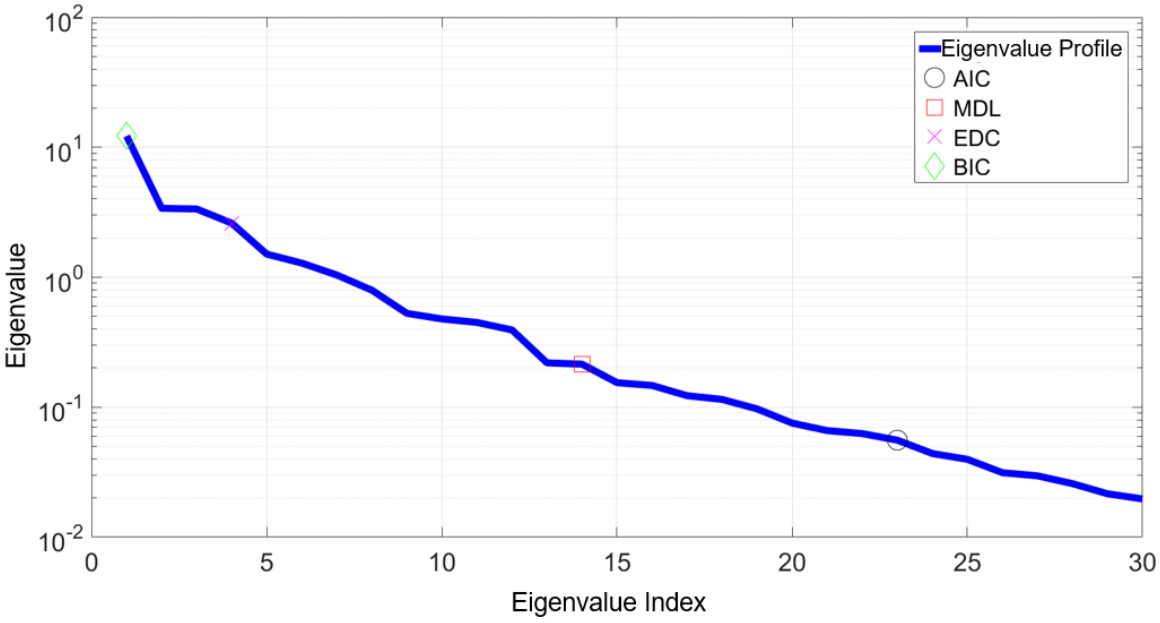

Figure 3.6 – Estimation of the amount of components using the state-of-the-art ITC shown in Subsection 3.3.2 using the main diagonal of the matrix $(\mathbf{\Sigma}_A)(1 : I_{max})$ of the measurements of block frequency at 3.84 Hz of the first volunteer.

In Figure 3.7, we apply the modified scheme using the most simplified expression proposed in Subsection 3.4.2. We observe that for the block frequency at 3.84 Hz, the estimates of AIC and MDL are the same.

For the second block frequency, we observe that AIC and MDL in Table 3.2 still provide an estimate according to the ICASSO range in Table 3.1. In case of the EDC and BIC, they only work for f_{s_2} and for the expression based on the eigenvalues of $(\mathbf{\Sigma}_A)(1 : I_{max})$ with an estimate similar to the MDL.

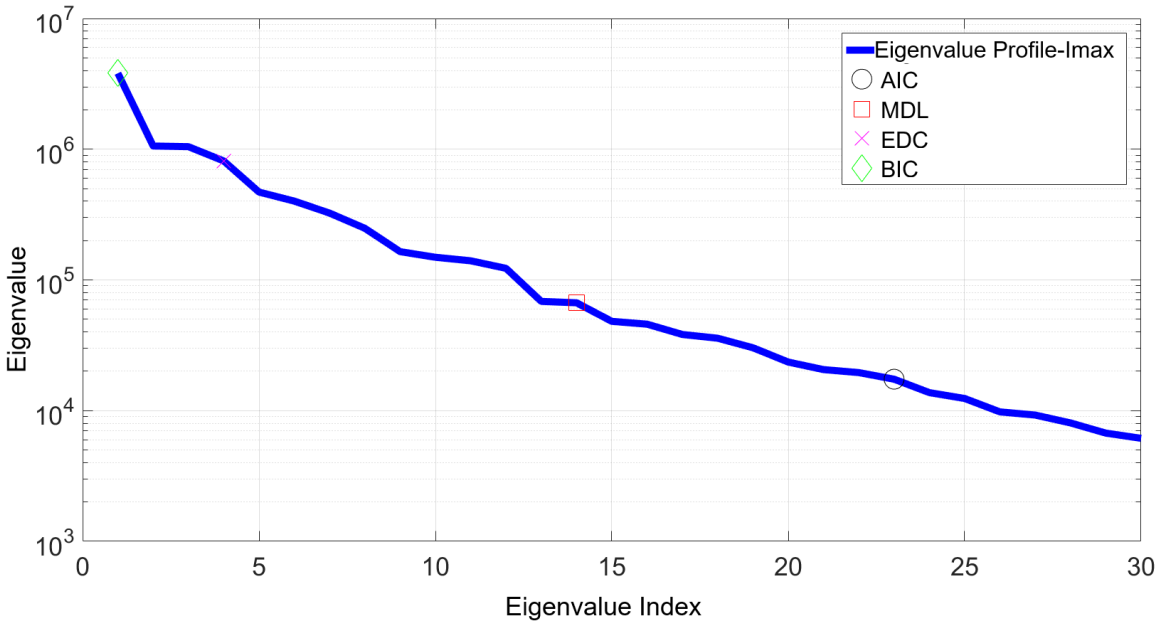

Figure 3.7 – Estimation of the amount of components using the state-of-the-art ITC shown in Subsection 3.3.2 using the main diagonal of the matrix $(\mathbf{\Sigma}_X)(1 : I_{max})$ of the measurements of block frequency at 3.84 Hz of the first volunteer.

Table 3.2 – Estimation of the amount of components of the MEG measurements via AIC and MDL.

	AIC			MDL		
	$diag(\mathbf{\Sigma}_A)$	$diag(\mathbf{\Sigma}_X)$		$diag(\mathbf{\Sigma}_A)$	$diag(\mathbf{\Sigma}_X)$	
		L_{max}	M		L_{max}	M
$f_{s_1} = 3.84$ Hz	23	23	64	14	14	64
$f_{s_2} = 21.73$ Hz	27	23	64	25	13	64

Table 3.3 – Estimation of the amount of components of the MEG measurements via EDC and BIC.

	EDC			BIC		
	$diag(\mathbf{\Sigma}_A)$	$diag(\mathbf{\Sigma}_X)$		$diag(\mathbf{\Sigma}_A)$	$diag(\mathbf{\Sigma}_X)$	
		L_{max}	M		L_{max}	M
$f_{s_1} = 3.84$ Hz	4	4	64	1	1	64
$f_{s_2} = 21.73$ Hz	25	4	64	25	1	64

3.5.2 Comparing schemes in terms of procesing time

Using a desktop computer with a processor of 2.6 GHz, the processing time of all algorithms is presented in Table 3.4. The ICASSO has the highest computational complexity due to the several FastICA realizations. As shown in in Table 3.4, the ICASSO processing time for a single block frequency is approximately 20 Minutes.

Still in Table 3.4, the traditional ITC present a very low computational complexity, although they completely fail for the estimation of the components as shown in Subsection 3.5.1. Therefore, in Table 3.4, the state-of-the-art ITC have an accuracy comparison with ICASSO as not OK (NOK).

The first scheme proposed in Section 3.4.1 presents a processing time of approximately 0.5 minute, which is almost 40 times faster than ICASSO. The second scheme proposed in Section 3.4.2 presents a processing time of approximately 0.18 second. Therefore, the second proposed scheme is almost seven times faster than ICASSO.

Table 3.4 – Comparison of the time processing for the proposed and state-of-the-art approaches

Approach	Absolute time processing	Relative value	Accuracy in comparison with ICASSO
ICASSO	1246.9 s $\approx$ 20.8 min	6927.2	OK
State-of-the-art ITC from Subsection 3.3.2 using d$iag(\mathbf{\Sigma}_X)(1:M)$	0.18 s	1	NOK
State-of-the-art ITC from Subsection 3.3.2 using d$iag(\mathbf{\Sigma}_X)(1:L_{max})$	0.18 s	1	OK
State-of-the-art ITC from Subsection 3.3.2 using d$iag(\mathbf{\Sigma}_A)(1:I_{max})$	31.0831 s $\approx$ 0.5 min	172.6	OK

3.6 SUMMARY OF THE LOW COMPLEXITY MODIFIED AIC

In this subsection, we summarize the steps to apply the modified AIC, since it presented the best performance in comparison to the other modified ITC approaches.

In order to estimate the model order of $\mathbf{X}^{\mathrm{s}}$ and $\mathbf{X}^{\mathrm{n}}$ in **Step 2** of Figure 3.1, we first decompose the matrices using the ICA into $I_{\mathrm{m}ax}$ components. Then, we reconstruct them in order to obtain the low rank approximations $\mathbf{X}^{\mathrm{s}'}$ and $\mathbf{X}^{\mathrm{n}'}$ using the $I_{\mathrm{m}ax}$ components. Next, we compute the sample covariance matrices of the low-rank approximations $\mathbf{X}^{\mathrm{s}'}$ and $\mathbf{X}^{\mathrm{n}'}$ as exemplified in (3.16) and (3.17).

$$\mathbf{R}^{\mathrm{s}} = \frac{\mathbf{X}^{\mathrm{s}'}}{\mathrm{I}_{max}} \in \mathbb{R}^{M \times M}, \tag{3.16}$$

$$\mathbf{R}^{\mathrm{n}} = \frac{\mathbf{X}^{\mathrm{n}'}}{\mathrm{I}_{max}} \in \mathbb{R}^{M \times M}. \tag{3.17}$$

Using the EVD, $\mathbf{R}^{\mathrm{s}}$ can be decomposed as Equation (3.18) and $\mathbf{R}^{\mathrm{n}}$ can be decomposed as Equation (3.19).

$$\mathbf{R}^{\mathrm{s}} = \mathbf{E}^{\mathrm{s}}\mathbf{\Lambda}^{\mathrm{s}}\mathbf{E}^{\mathrm{s}^{\mathrm{T}}}, \tag{3.18}$$

$$\mathbf{R}^{\mathrm{n}} = \mathbf{E}^{\mathrm{n}}\mathbf{\Lambda}^{\mathrm{n}}\mathbf{E}^{\mathrm{n}^{\mathrm{T}}}, \tag{3.19}$$

where $\mathbf{E}^{\mathrm{s}}$ and $\mathbf{E}^{\mathrm{n}}$ are the matrices with eigenvectors, while $\mathbf{\Lambda}^{\mathrm{s}}$ and $\mathbf{\Lambda}^{\mathrm{n}}$ are diagonal matrices with eigenvalues. In order to estimate the model orders of data with and without measurements, we apply the eigenvalue vectors on (3.20) by computing $\mathrm{diag}(\mathbf{\Lambda}^{\mathrm{s}})$ and $\mathrm{diag}(\mathbf{\Lambda}^{\mathrm{n}})$.

$$J(k) = -I_{\mathrm{max}}(I_{\mathrm{max}} - k)\log\left(\frac{g(k)}{a(k)}\right) + p(k, I_{\mathrm{max}}, I_{\mathrm{max}}), \tag{3.20}$$

where $g(k)$ is the geometric mean of the k smallest eigenvalues, $a(k)$ is the arithmetic mean of the k smallest eigenvalues and $p(k, I_{\mathrm{max}}, I_{\mathrm{max}}) = k(2I_{\mathrm{max}} - k)$.

By using the $\mathrm{diag}\,(\mathbf{\Lambda}^{\mathrm{s}})$ in Equation (3.20), we obtain the estimated model order I^s, while by using the $\mathrm{diag}\,(\mathbf{\Lambda}^{\mathrm{n}})$ in Equation (3.20), we obtain the estimated model order I^n.

3.7 PROPOSED UNSUPERVISED FRAMEWORK FOR THE IDENTIFICATION

Inspired by our previous contributions in [10, 9, 55], we propose three approaches in Subsubsection 3.7.2 to identify the VEP components from the ICA components computed in **Step 3** of Figure 3.1. In order to apply the three unsupervised identification approaches in an automatic fashion, we propose a calibration scheme in Subsubsection 3.7.1.

The according to **Step 4** in Figure 3.1, the inputs of **Step 4** in Figure 3.1 are the matrices $\mathbf{A}^{\mathrm{s}}$, $\mathbf{A}^{\mathrm{n}}$, $\mathbf{S}^{\mathrm{s}}$, and $\mathbf{S}^{\mathrm{n}}$. Still according to **Step 4** in Figure 3.1, the independent components from the measurements without stimulation are used to calibrate the unsupervised identification approaches, finding the parameter τ for each approach.

Note that according to the **Step 4** in Figure 3.1, each approach uses different information

from the independent components in order to identify the VEP components. In the unsupervised identification 1 for unsupervised comparison, the matrices $\mathbf{A}^{\mathrm{s}}$ and $\mathbf{A}^{\mathrm{n}}$ are used to identify the VEP components. In the unsupervised identification 2, the columns of the matrix $\mathbf{A}^{\mathrm{s}}$ and $\mathbf{A}^{\mathrm{n}}$ are mapped into the frequency domain by applying the Discrete Fourier Transform (DFT) matrix $\mathbf{W}$. Finally, the unsupervised identification 3 uses the matrices $\mathbf{S}^{\mathrm{s}}$ and $\mathbf{S}^{\mathrm{n}}$ for the unsupervised identification of the VEP components.

Since the three calibration schemes have the same principle and without loss of generality, we have the matrices $\mathbf{\Psi}^{\mathrm{s}} = \mathbf{A}^{\mathrm{s}}$ and $\mathbf{\Psi}^{\mathrm{n}} = \mathbf{A}^{\mathrm{n}}$ in case of the unsupervised identification 1, the matrices $\mathbf{\Psi}^{\mathrm{s}} = |\mathbf{W}\mathbf{A}^{\mathrm{s}}|$ and $\mathbf{\Psi}^{\mathrm{n}} = |\mathbf{W}\mathbf{A}^{\mathrm{n}}|$ in case of the unsupervised identification 2 and the matrices $\mathbf{\Psi}^{\mathrm{s}} = \left|\mathbf{W}\mathbf{S}^{\mathrm{s}^{\mathrm{T}}}\right|$ and $\mathbf{\Psi}^{\mathrm{n}} = \left|\mathbf{W}\mathbf{S}^{\mathrm{n}^{\mathrm{T}}}\right|$ in case of the unsupervised identification 3.

3.7.1 Calibration scheme to determine the threshold value τ

In order to find the threshold parameter τ, we compute the angular distance between two vectors with indices p and q of the matrix $\mathbf{\Psi}^{\mathrm{n}}$:

$$\phi^{\mathrm{n}}_{p,q} = \frac{2}{\pi} \cdot \arccos \left| \left(\frac{\mathbf{\Psi}^{\mathrm{n}}(:,p)}{\|\mathbf{\Psi}^{\mathrm{n}}(:,p)\|} \right)^{\mathrm{T}} \frac{\mathbf{\Psi}^{\mathrm{n}}(:,q)}{\|\mathbf{\Psi}^{\mathrm{n}}(:,q)\|} \right|, \tag{3.21}$$

where $p = 1, \cdots, I^n$ and $q = 1, \cdots, I^n$ and $p \neq q$. The value $\phi^{\mathrm{n}}_{p,q}$ is normalized to define the angular distance between 0 and 1. Note that each p-th vector is compared to I_{n-1} vectors.

Next, we compute (3.22) for each p-th vector. Note that $\phi^{n}_{p,\mathrm{min}}$ provides minimum angular distance p-th vector and the other remaining vectors. In case that the vector is related to the VEP components, we assume that the pattern of the vector is different from all other vectors, implying into a greater $\phi^{n}_{p,\mathrm{min}}$.

$$\phi^{n}_{p,\mathrm{min}} = \min(\phi^{n}_{\mathrm{p},:}). \tag{3.22}$$

Since $\mathbf{\Psi}^{\mathrm{n}}$ is obtained from non-stimulated measurements, an average angular distance value is expected. Finally, the calibration parameter τ is computed in (3.23).

$$\tau = \max(\phi^{n}_{\mathrm{min}}). \tag{3.23}$$

3.7.2 Unsupervised identification using the calibration parameter τ

Similar to the calibration approach in Subsubsection 3.7.1, the first step for the identification of the VEP components is to compute the angular distance between the vectors of the

$\mathbf{\Psi}^{\mathrm{n}}$ and the vectors of the matrix $\mathbf{\Psi}^{\mathrm{n}}$.

$$\phi^{\mathrm{s}}_{p,q} = \frac{2}{\pi} \cdot \arccos \left| \left(\frac{\mathbf{\Psi}^{\mathrm{s}}(:,p)}{\|\mathbf{\Psi}^{\mathrm{s}}(:,p)\|} \right)^{\mathrm{T}} \frac{\mathbf{\Psi}^{\mathrm{n}}(:,q)}{\|\mathbf{\Psi}^{\mathrm{n}}(:,q)\|} \right|, \tag{3.24}$$

where $p = 1, \cdots, I^s$ and $q = 1, \cdots, I^n$ and $p \neq q$. The value $\phi^{\mathrm{s}}_{p,q}$ is normalized to define the angular distance between 0 and 1.

Similar to Subsubsection 3.7.1, each p-th vector is compared to $I^s - 1$ vectors. Next, we compute (3.25) for each p-th vector. Note that $\phi^{s}_{p,\mathrm{min}}$ provides minimum angular distance p-th vector and the other remaining vectors.

$$\phi^{s}_{p,\mathrm{min}} = \min(\phi^{s}_{\mathrm{p},:}). \tag{3.25}$$

In contrast to Subsubsection 3.7.1, we compare $\phi^{s}_{p,\mathrm{min}}$ to the calibration parameter τ. If (3.26) holds true, then it is assumed that the p-th vector belongs to a VEP component. The procedure is repeated for all I_s vectors. The output of the three unsupervised identification approaches are a set of indices related to VEP-independent components.

$$\phi^{s}_{p,\mathrm{min}} > \tau. \tag{3.26}$$

3.7.3 Subjective VEP identification via visual inspection

In order to perform the subject VEP identification via visual inspection, two approaches are applied, namely, average amplitude spectrum and spectral topography. We depict the average amplitude spectrum and spectral topography in Subsection 3.8.2.

To improve the performance of the average amplitude spectrum and spectral topography, we process the data applying the resolution r and overlap l parameters according to **Step 5** of Figure 3.1.

The resolution r is the amount of flash periods in each segment. Therefore, if $r = 1$, it means that each segment has only P samples, which is the amount of samples in each flash period. Since each row has size $P \cdot N_w \cdot N_z$, the matricization process by varying r, provides an output matrix of size: $P \cdot r \times \frac{N_w \cdot N_z}{r}$.

The overlap l is the amount of samples that are repeated from each consecutive vector. For instance, in case that $l = 0.1$, it means 10 % overlap between two consecutive vectors. Therefore, by using the parameters r and l, we obtain a trial matrix of size $P \cdot r \times \frac{N_w \cdot N_z}{r(1-l)}$. Still in **Step 5** of Figure 3.1, each segment of size $p \cdot r$ is multiplied by a Hanning window to avoid the leakage effect.

3.7.4 Decision fusion based on the outputs of all approaches

In order to fuse the outputs of the approaches, we use set operations, such as unions and intersections. In the case of union operation, we assume the non-detection, *i.e.*, some approaches have not been able to identify the VEP components identified by the other approaches. Therefore, by combining the outputs of the approaches, we include the non-detected VEP components. In the case of intersection operation, we assume a false alarm, *i.e.*, some approaches mistakenly identified a non-VEP component as a VEP component. Therefore, by applying the intersection, we expect that the non-VEP component is removed from the set of components.

3.8 EXPERIMENTAL RESULTS

This section presents the results obtained using the automatic procedures and subjective VEP identification by visual inspection. In Subsection 3.8.1, the validation of the τ parameter is discussed in detail. Then, in Subsection 3.8.2, an in-depth analysis of the automated procedure is carried out. The results of the subjective identification of the VEP by visual inspection are presented in Subsection 3.8.3. Finally, in Subsection 3.8.4, the decision fusion of the results of all the approaches is presented.

3.8.1 Calculation and validation of τ parameter

Through the calibration, which is applied to $\mathbf{\Psi}^{\mathrm{s}}$ derived from the measurements with stimulation, the threshold parameter τ varies within the range of 0.65 to 0.85. Consequently, τ can be a parameter for identifying the VEP components. In the case of $\mathbf{\Psi}^{\mathrm{n}}$, τ falls within the range of approximately 0.55 to 0.65.

In Figures 3.8 and 3.9, we depict the histogram of $\phi^{n}_{p,\mathrm{min}}$ obtained from Equation (3.22).

By applying the histogram and as depicted in Figure 3.8, the $\max(\phi^{n}_{p,\mathrm{min}})$ is a value ranging around 0.6. Therefore, τ can be chosen to a value close to 0.6.

As depicted in Figure 3.9, the $\max(\phi^{n}_{p,\mathrm{min}})$ is a value ranging around 0.5. Therefore, τ can be chosen to a value close to 0.5 for these measurements. However, in order to consider a more conservative scenario, $\tau = 0.6$ is used in the unsupervised identification approaches.

In Figures 3.10 and 3.11, we depict the histogram of $\phi^{s}_{p,\mathrm{min}}$ obtained from Equation (3.25). Note that the stimulation frequency considered is 3.84 Hz.

As depicted in Figure 3.10, the $\max(\phi^{s}_{p,\mathrm{min}})$ is a value ranging around 0.7. Therefore, since $\tau = 0.6$, several components whose $\phi^{s}_{p,\mathrm{min}}$ are greater than 0.6 are identified.

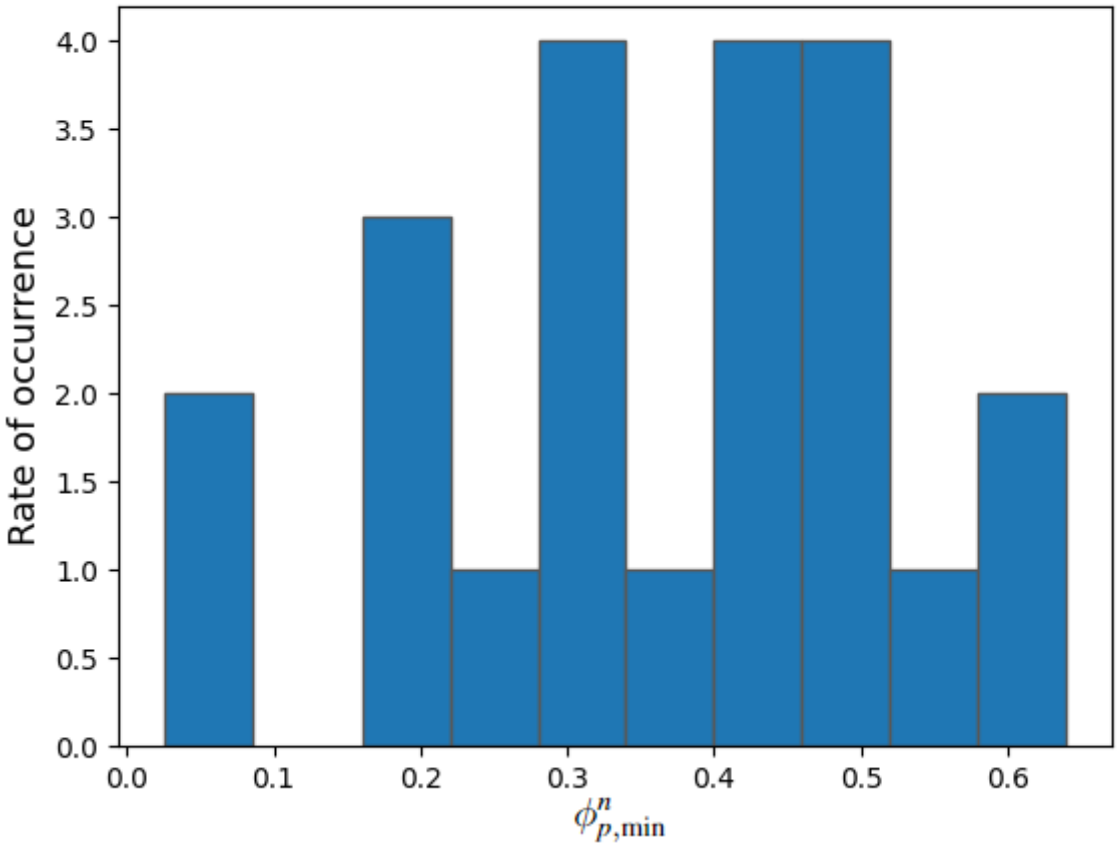

Figure 3.8 – Histogram of the $\phi^n_{p,\min}$ obtained from Equation (3.22). Note that $\tau \approx 0.6$ for the data without stimulation

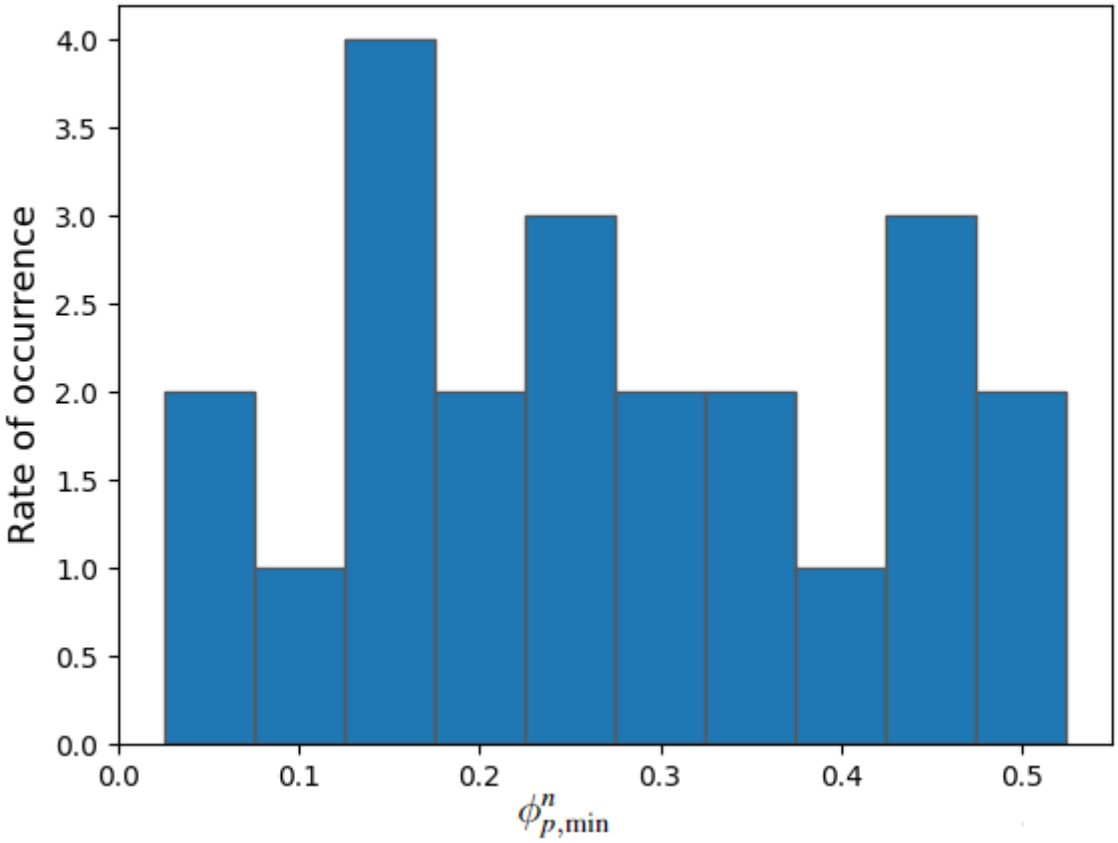

Figure 3.9 – Histogram of the $\phi^n_{p,\min}$ obtained from Equation (3.22). Note that $\tau \approx 0.5$ for the data without stimulation

As depicted in Figure 3.11, the $\max(\phi^s_{p,\min})$ is a value ranging around 0.8. Therefore, since $\tau = 0.6$, several components whose $\phi^s_{p,\min}$ are greater than 0.6 are identified.

3.8.2 Automatic unsupervised VEP identification

In Table 3.5, we have the results of the application of the three unsupervised identification approaches considering three different stimulation frequencies, namely, $f_{s1} = 3.84$ Hz, $f_{s2} = 21.73$ Hz, and $f_{s3} = 19.23$ Hz.

In the column r_{u1} of Table 3.5, we present the indices of the found VEP components applying the unsupervised identification 1 for three different stimulation frequencies. We can realize that the amount of VEP components are ranging from one to six given the outputs of f_s1 and f_s2.

In the column r_{u2} of Table 3.5, we present the indices of the found VEP components applying the unsupervised identification 2 for three different stimulation frequencies. We can realize that the VEP components are varying from one in case of f_{s3} and six in the case

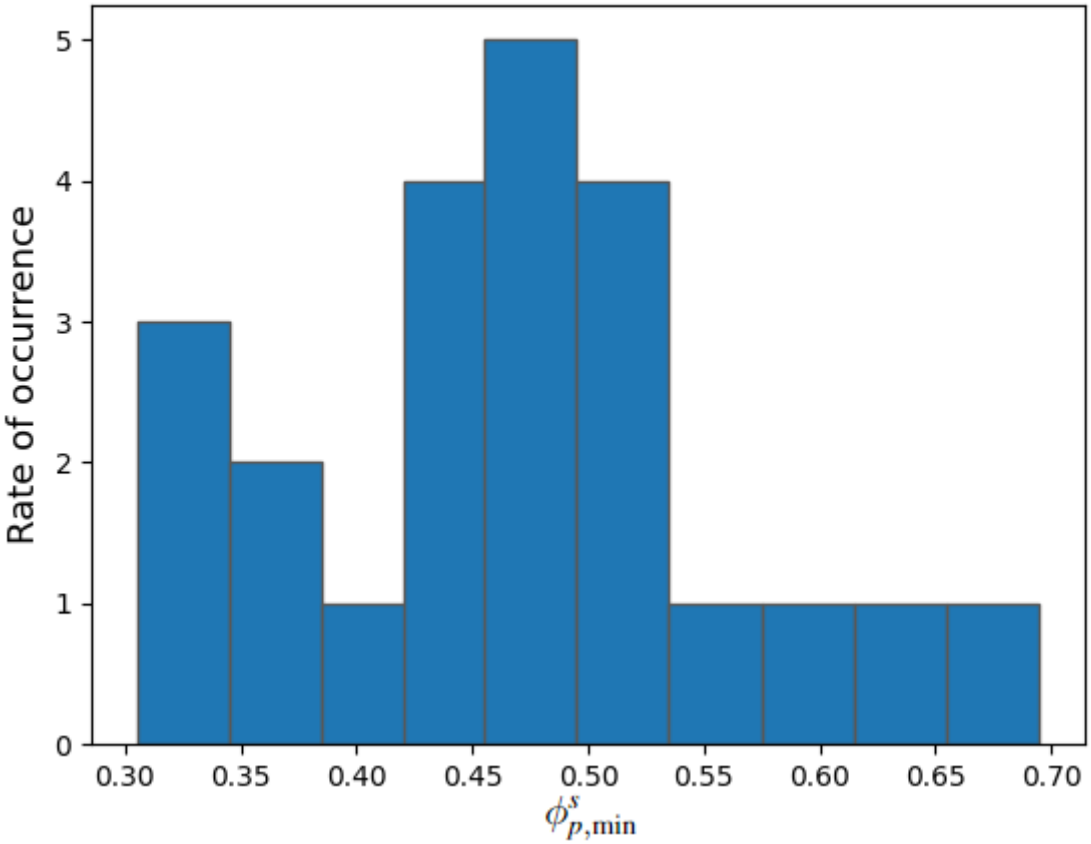

Figure 3.10 – Histogram of the $\phi^s_{p,\min}$ obtained from Equation (3.25). Note that $\tau \approx 0.7$ for the data with stimulation

of f_{s2}.

In the column r_{u3} of Table 3.5, we present the indices of the found VEP components applying the unsupervised identification 3 for three different stimulation frequencies. We can realize that the VEP components are varying from two in case of f_{s1} and f_{s3}, and none in the case of f_{s2}. Note that, in case of no VEP component, the symbol of empty set ($\varnothing$) is used.

	$\mathbf{r}_{u1}$	$\mathbf{r}_{u2}$	$\mathbf{r}_{u3}$
f_{s1} = 3.84 Hz	5	5, 8, 9	20, 23
f_{s2} = 21.73 Hz	1, 2, 4, 6, 12, 23	1, 2, 4, 9, 12, 20	$\varnothing$
f_{s3} = 19.23 Hz	5, 9, 15, 17, 21	3	1, 9

Table 3.5 – Indices of the identified VEP independent components using the three unsupervised approaches considering three stimulation frequencies, namely, f_{s1}, f_{s2}, and f_{s3}

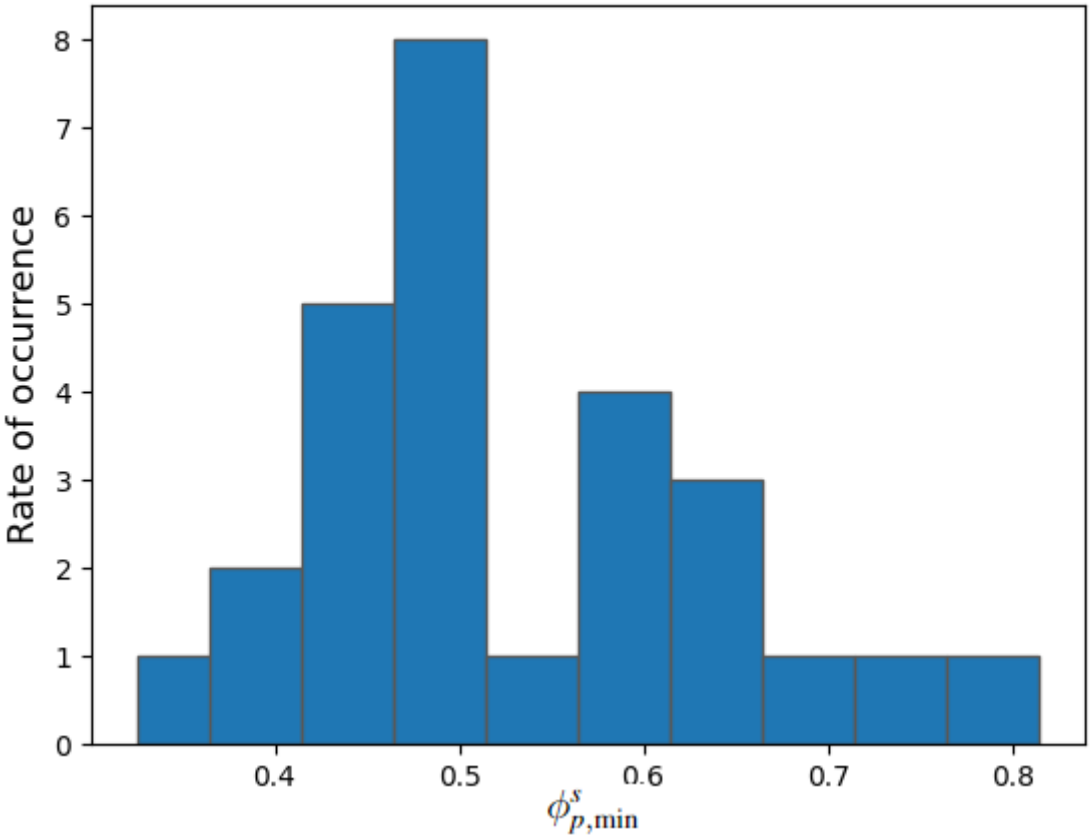

Figure 3.11 – Histogram of the $\phi^s_{p,\min}$ obtained from Equation (3.25). Note that $\tau \approx 0.85$ for the data with stimulation

3.8.3 Subjective VEP Identification via Visual Inspection

For **Step 5** of Figure 3.1, the obtained recording of the components of each measurement is visually estimated concerning the component number of AIC. First, the mean values of the amplitude spectrum of the MEG channels 50 to 102 of each component are estimated, and the measurement components from the first subject with different stimulation frequencies are analyzed. For this purpose, a VEP component is considered if a peak is presented at least at the particular stimulation or harmonic frequencies.

Figure 3.12 exemplifies the visual inspection of the mean value of the amplitude spectrum for the independent component with index $p = 2$ of the measurements with stimulation frequency $f_{s1} = 3.84$ Hz. Note that there is a peak in the frequency f_{s1}. Therefore, the independent component with $p = 2$ can be identified as VEP using the criterion of average amplitude spectrum.

In Figure 3.13, the independent component with index $p = 6$ presents two peaks on the frequencies f_{s1} and f_{s2}. Therefore, the independent component with $p = 6$ can be identified

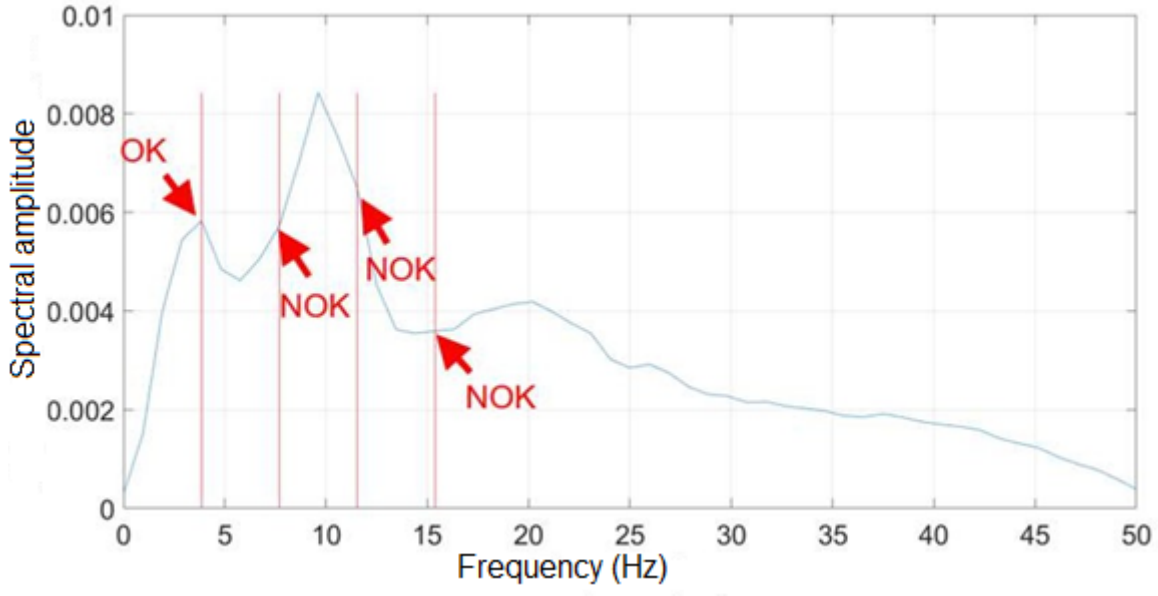

Figure 3.12 – Mean value of the amplitude spectrum of the independent component with $p = 2$ considering a stimulation $f_{s1} = 3.84$ Hz. Note that the independent component with $p = 2$ can be identified as VEP using this criterion

as VEP using the criterion of average amplitude spectrum.

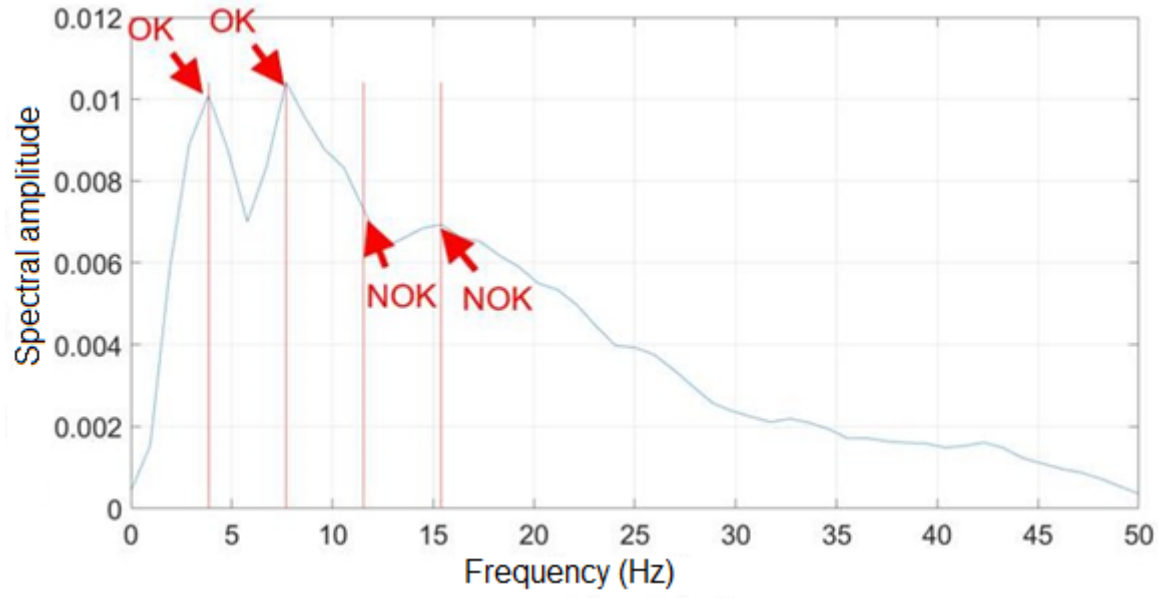

Figure 3.13 – Mean value of the amplitude spectrum of the independent component with $p = 6$ considering a stimulation $f_{s1} = 3.84$ Hz. Note that the independent component with $p = 2$ can be identified as VEP using this criterion

In Figures 3.14 and 3.15, we exemplify the spectral topography. By the visual topography, we marked in red line the area of the sensors related to the visual cortex. Therefore, in case that this region is more activated than the other regions, the independent component can be considered as a VEP component.

In Figure 3.14, we have the spectral topography of the independent component with $p = 2$. Since the region of the visual cortex presents a small power, we cannot consider it as a VEP component using the criterion of the visual inspection of the spectral topography.

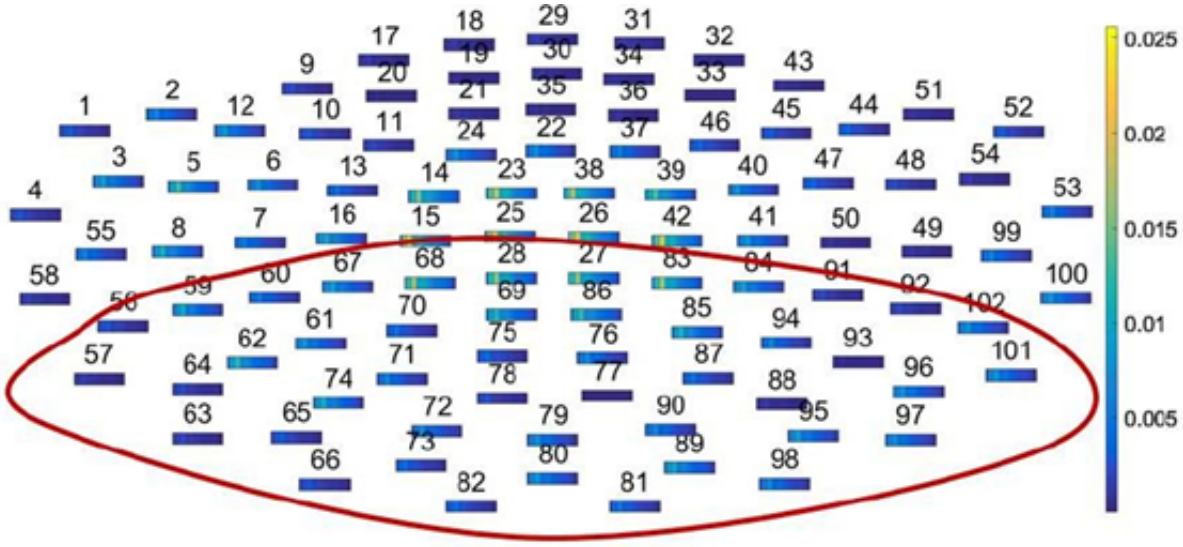

Figure 3.14 – Spectral topography of the independent component with $p = 2$ considering a stimulation $f_{s1} = 3.84$ Hz. Note that the independent component with $p = 2$ cannot be identified as VEP using this criterion

On the other hand, in Figure 3.15, we have the spectral topography of the independent component with $p = 6$. Since the region of the visual cortex is slightly activated, we can consider it as a VEP component using the criterion of the visual inspection of the spectral topography.

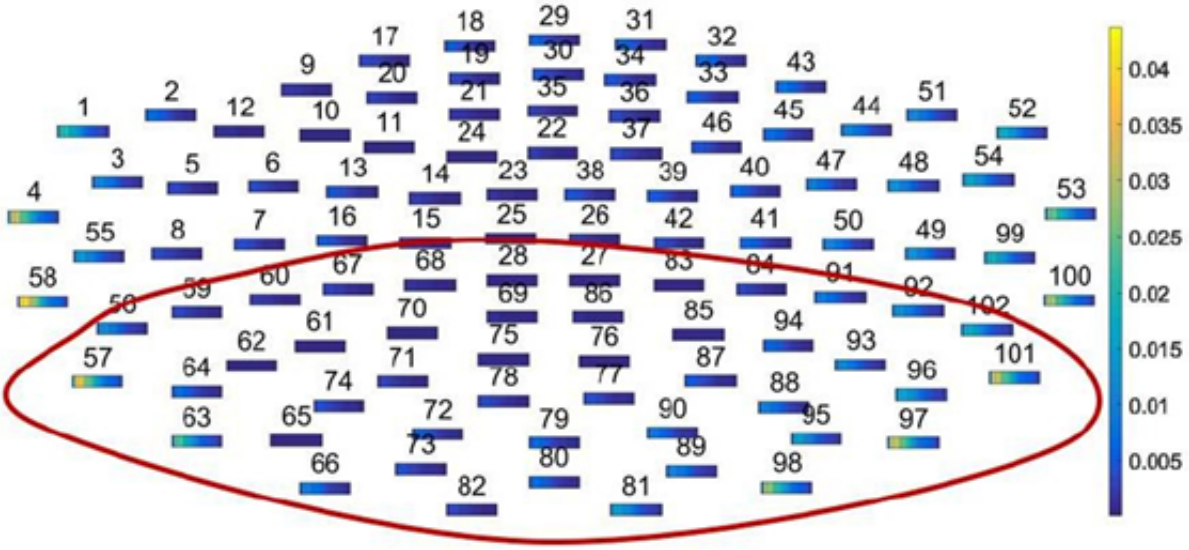

Figure 3.15 – Spectral topography of the independent component with $p = 6$ considering a stimulation $f_{s1} = 3.84$ Hz. Note that the independent component with $p = 6$ can be identified as VEP using this criterion

Table 3.6 displays the indices p of the identified VEP components through visual inspec-

tion of the mean values of the amplitude spectrum and spectral topographies. By fusing the sets of the two visual inspection approaches using intersection, we obtain the indices displayed in the last column of Table 3.6.

	$\mathbf{r}_{v1}$	$\mathbf{r}_{v2}$	$\mathbf{r}_{v1} \cap \mathbf{r}_{v2}$
f_{s1} = 3.84 Hz	2, 3, 4, 5, 6, 7, 8, 10, 11, 15, 16, 17, 18, 20, 21	1, 3, 4, 6, 7, 8, 9,10, 15, 16, 17, 18, 20, 23	3, 4, 6, 7, 8, 10 15, 16, 17, 18, 20
f_{s2} = 21.73 Hz	1, 4, 6, 8, 12, 13, 16	1, 3, 4, 6, 8, 9, 10, 12, 14, 16, 17, 19, 20, 21, 22	1, 4, 6, 8, 12, 16
f_{s3} = 19.23 Hz	2, 3, 4, 8, 9, 11, 12, 14, 18	1, 2, 3, 4, 6, 7, 8, 9, 10, 13, 14, 16, 17, 21, 22	2, 3, 4, 8, 9, 14

Table 3.6 – Indices of the identified VEP independent components using two visual inspection approaches considering three stimulation frequencies, namely, f_{s1}, f_{s2}, and f_{s3}. Example of the decision fusion applying the intersection operation

3.8.4 Decision fusion based on the outputs of all approaches

According to Section 3.7.4, the decision fusion of the independent components can be applied using set operations. In this subsection, we present only the usage of the intersection operator.

In Table 3.7, we present the outputs of the three unsupervised identification approaches, of the intersection of the two visual inspection approaches, and of the intersection of the visual inspection intersection and of each unsupervised identification approach. Column 5 shows the intersection operations (called $\mathbf{r}_v$) between the visual inspection outputs ($\mathbf{r}_{v1} \cap \mathbf{r}_{v2}$). Columns 6, 7 and 8 show the intersection operations between the automated procedures and the visual inspection. Column 6, unsupervised identification 1 and the intersection with the subjective identification of the VEP through visual inspection. Similarly, columns 7 and 8, unsupervised identification 2 and 3, respectively, reflect the intersections with the subjective identification of the VEP via visual inspection.

	$\mathbf{r}_{u1}$	$\mathbf{r}_{u2}$	$\mathbf{r}_{u3}$	$\mathbf{r}_{v1} \cap \mathbf{r}_{v2} = \mathbf{r}_v$	$\mathbf{r}_{u1} \cap \mathbf{r}_v$	$\mathbf{r}_{u2} \cap \mathbf{r}_v$	$\mathbf{r}_{u3} \cap \mathbf{r}_v$
f_{s1} = 3.84 Hz	5	5, 8, 9	20, 23	3, 4, 6, 7, 8, 10 15, 16, 17, 18, 20	$\varnothing$	8	20
f_{s2} = 21.73 Hz	1, 2, 4, 6, 12, 23	1, 2, 4, 9, 12, 20	$\varnothing$	1, 4, 6, 8, 12, 16	1, 4, 6, 12	1, 4, 12	$\varnothing$
f_{s3} = 19.23 Hz	5, 9, 15, 17, 21	3	1, 9	2, 3, 4, 8, 9, 14	9	3	9

Table 3.7 – Indices of the identified VEP independent components using the three unsupervised identification approaches and the intersection of the two visual inspection approaches considering three stimulation frequencies, namely, f_{s1}, f_{s2}, and f_{s3}. Example of the decision fusion applying the tree different intersection operations

3.9 SUMMARY OF THE CHAPTER

One crucial step in the VEP analysis from EEG or MEG measurements is the selection of the amount of components before applying BSS schemes, such as the . The state-of-the-art approach ICASSO has a significant computational complexity and the dependence of human intervention to define thresholds in order to correctly find the amount of resolvable components. On the other hand, traditional eigenvalue based information ITC, such as AIC and MDL completely fail to directly estimate the amount of components from the MEG measurements.

In this work, we propose a modification of the traditional eigenvalue based ITC, such that an estimate of the amount of components are similar to the ICASSO can be achieved. Moreover, the modified ITC presents a dramatic reduce in the computational cost in comparison with ICASSO.

In this chapter, we propose an unsupervised framework for the identification of VEP in MEG measurements. The proposed framework can be used to replace or to complement the traditional visual inspection based approaches. Moreover, in contrast to the current supervised machine learning schemes, the proposed framework does not require any training data set. The presented results are validated using measurements from the Jena University Hospital. By applying the ICASSO in the measurements, a total of 23 components are estimated. We validate our results using MEG measurements.

4 CONCLUSIONS

In this chapter, we draw the conclusions and we provide next research topics. Four main contributions related to overall objective of developing software and hardware solutions for biomedical engineering applications, in particular, array signal processing techniques, are presented. First a MWHD, including high-resolution signal processing algorithms to measure of the Heart Rate (HR) and the steps is proposed. Second traditional eigenvalue based ITC are modified to estimate the amount of components of MEG and EEG data. Third an unsupervised framework for the identification of VEP in MEG measurements is proposed. Finally, we validate the results with measurements.

In this thesis, hardware and software solutions for biomedical engineering applications are proposed.

Chapter 2 presents a complete framework for health systems composed of MWHD, high-resolution parameter estimation, and real-time monitoring application. The system can be further improved by using novel sensors and by incorporating a for the fast processing of the data.

Chapter 3 proposes unsupervised frame- work for the identification of VEP in MEG measurements, including a solution for the MOS. The proposed framework can be further improved by exploiting also supervised machine learning algorithms. In this case, labeled data is necessary. Therefore, a pre-processing of the measurements with the support of an expert or the usage of a labeled data base is essential.

The contributions in the Appendices A, C and D can also be further developed by incorporating more sophisticated array signal processing. With respect to Appendix A, machine learning algorithms that exploit the natural tensor structure can be proposed. In Appendix C, additional sensors can be combined in order to increase the accuracy. In this case, multimensional array signal processing schemes can also be exploited. Finally, in Appendix D, the data of each array is individually processed. In order to further improve the solution, a novel tensor-based framework with jointly processing of the data of the arrays can be applied.

BIBLIOGRAPHY

1 HASSANALIERAGH, M.; PAGE, T. S. A.; SHARMA, G.; AKTAS, G. M. M.; KANTARCI, B.; ANDREESCU, S. Health monitoring and management using internet-of-things (iot) sensing with cloud-based processing: Opportunities and challenges. In: *IEEE International Conference on Services Computing*. [S.l.: s.n.], 2015. p. 285–292.

2 PANTELOPOULOS, A.; BOURBAKIS, N. A survey on wearable sensor-based systems for health monitoring and prognosis. *IEEE Trans. Sys., Man, and Cybernetics, Part C: Applic. and Reviews*, v. 40, p. 1–12, 2010.

3 PRETTZ, J. B.; COSTA, J. P. C. L. da; ZANATTA, M. R.; ALVIM, J. R.; MIRANDA, R. K. Efficient and low cost mimo communication architecture for smartbands applied to postoperative patient care. In: *2nd Russian-Pacific Conference on Computer Technology and Applications (RPC-2017)*. [S.l.: s.n.], 2017. p. 1–5.

4 PINHEIRO, G. P. M.; MIRANDA, R. K.; PRACIANO, B. J. G.; SANTOS, G. A.; MENDONÇA, F. L. L.; JAVIDI, E.; COSTA, J. P. C. L. da; SOUSA JÚNIOR, R. T. de. Multi-sensor wearable health device framework for real-time monitoring of elderly patients using a mobile application and high-resolution parameter estimation. *Frontiers in Human Neuroscience*, v. 15, p. 1–12, 2022.

5 MARANHÃO, J. P. A.; COSTA, J. P. C. L. da; FREITAS, E. P. de; JAVIDI, E.; SOUSA JÚNIOR, R. T. de. Error-robust distributed denial of service attack detection based on an average common feature extraction technique. *Sensors*, v. 20, p. 1–21, 2020.

6 MARANHÃO, J. P. A.; COSTA da; L., J. P. C.; FREITAS, E. P. de; JAVIDI, E.; SOUSA JÚNIOR, R. T. de. Noise-robust multilayer perceptron architecture for distributed denial of service attack detection. *IEEE Commuications Letters*, v. 25, p. 402–406, 2020.

7 MARANHÃO, J. P. A.; COSTA, J. P. C. L. da; FREITAS, E. P. de; JAVIDI, E.; BORGES, C. A.; SOUSA JÚNIOR, R. T. de. Tensor based framework for distributed denial of service attack detection. *Journal of Network and Computer Applications*, v. 174, p. 1–15, 2021.

8 MARANHÃO, J. P. A.; COSTA, J. P. C. L. da; JAVIDI, E.; SOUSA JÚNIOR, R. T. de; MILANEZI JÚNIOR, J. Multidimensional antenna array based framework for drone localization in multipath environments. In: *International Conference on Signal Processing and Communication Systems (ICSPCS)*. [S.l.: s.n.], 2019.

9 JAVIDI, E.; COSTA, J. P. C. L. da; MIRANDA, R. K.; MARANHÃO, J. P. A.; VARGAS, J. A. R. Modified information theoretic criteria for low complexity estimation of the amount of components in meg measurements. In: *International Conference on Signal Processing and Communication Systems (ICSPCS)*. [S.l.: s.n.], 2019.

10 JAVIDI, E.; COSTA, J. P. C. L. da; MIRANDA, R. K.; MARANHÃO, J. P. A.; VARGAS, J. A. R. Unsupervised framework for the identification of visual evoked potential in meg measurements. In: *International Conference on Signal Processing and Communication Systems (ICSPCS)*. [S.l.: s.n.], 2019.

11 REGA, D. G.; MIRANDA, R. K.; JAVIDI, E.; MARANHÃO, J. P. A.; COSTA, J. P. C. L. da; PINHEIRO, G. P. Esprit-based step count for wearable devices. In: *International Conference on Signal Processing and Communication Systems (ICSPCS)*. [S.l.: s.n.], 2019.

12 PHUA, J.; WENG, L.; LING, L.; EGI, M.; LIM, C.-M.; DIVATIA, J. V.; SHRESTHA, B. R.; ARABI, Y. M.; NG, J.; GOMERSALL, C. D.; NISHIMURA, M.; KOH, Y.; DU, B. Intensive care management of coronavirus disease 2019 (covid-19): challenges and recommendations. *The Lancet Respiratory Medicine*, Elsevier, v. 8, n. 5, p. 506–517, May 2020. ISSN 2213-2600. Disponível em: <https://doi.org/10.1016/S2213-2600(20)30161-2>.

13 ALWASHMI, M. F. The use of digital health in the detection and management of covid-19. *International Journal of Environmental Research and Public Health*, Multidisciplinary Digital Publishing Institute, v. 17, n. 8, p. 1–7, 2020.

14 WEARABLE Medical Device Market Size, Share & Trends Analysis Report By Product Type (Diagnostic, Therapeutic, Respiratory), By Site (Strap/Clip/Bracelet, Handheld), By Application, And Segment Forecasts, 2020 - 2027. [S.l.], 2020. 150 p. Disponível em: <https://www.grandviewresearch.com/industry-analysis/wearable-medical-devices-market/segmentation>.

15 MARINHO, M. A. M.; FREITAS, E. P. de; COSTA, J. P. C. L. da; ALMEIDA, A. L. F. de; SOUSA JÚNIOR, R. T. de. Using cooperative mimo techniques and uav relay networks to support connectivity in sparse wireless sensor networks. In: *2013 International Conference on Computing, Management and Telecommunications (ComManTel)*. [S.l.: s.n.], 2013. p. 49–54.

16 FREITAS, E. P. de; COSTA, J. P. C. L. da; ALMEIDA, A. L. F. de; MARINHO, M. Applying mimo techniques to minimize energy consumption for long distances communications in wireless sensor networks. In: ANDREEV, S.; BALANDIN, S.; KOUCHERYAVY, Y. (Ed.). *Internet of Things, Smart Spaces, and Next Generation Networking*. Berlin, Heidelberg: Springer Berlin Heidelberg, 2012. p. 379–390. ISBN 978-3-642-32686-8.

17 WU, T.; WU, F.; QIU, C.; REDOUTE, J.-M.; YUCE, M. R. A Rigid-Flex Wearable Health Monitoring Sensor Patch for IoT-Connected Healthcare Applications. *IEEE Internet of Things Journal*, p. 1–1, 2020. ISSN 2327-4662, 2372-2541. Disponível em: <https://ieeexplore.ieee.org/document/9018016/>.

18 PURANIK, S.; MORALES, A. W. Heart Rate Estimation of PPG Signals With Simultaneous Accelerometry Using Adaptive Neural Network Filtering. *IEEE Transactions on Consumer Electronics*, v. 66, n. 1, p. 69–76, 02 2020. ISSN 0098-3063, 1558-4127. Disponível em: <https://ieeexplore.ieee.org/document/8937489/>.

19 CHUNG, H.; KO, H.; LEE, H.; LEE, J. Deep Learning for Heart Rate Estimation From Reflectance Photoplethysmography With Acceleration Power Spectrum and Acceleration Intensity. *IEEE Access*, v. 8, p. 63390–63402, 2020. ISSN 2169-3536. Disponível em: <https://ieeexplore.ieee.org/document/9042276/>.

20 PANWAR, M.; GAUTAM, A.; BISWAS, D.; ACHARYYA, A. PP-Net: A Deep Learning Framework for PPG based Blood Pressure and Heart Rate Estimation. *IEEE*

Sensors Journal, v. 20, p. 10001–10011, 2020. ISSN 1530-437X, 1558-1748, 2379-9153. Disponível em: <https://ieeexplore.ieee.org/document/9082808/>.

21 COFFEN, B.; SCOTT, P.; MAHMUD, M. S. Real-time Wireless Health Monitoring: An Ultra-low Power Biosensor Ring for Heart Disease Monitoring. In: *2020 International Conference on Computing, Networking and Communications (ICNC)*. Big Island, HI, USA: IEEE, 2020. p. 626–630. ISBN 978-1-72814-905-9. Disponível em: <https://ieeexplore.ieee.org/document/9049814/>.

22 WANG, M.; LI, Z.; ZHANG, Q.; WANG, G. Removal of motion artifacts in photoplethysmograph sensors during intensive exercise for accurate heart rate calculation based on frequency estimation and notch filtering. *Sensors*, v. 19, n. 15, 2019. ISSN 1424-8220. Disponível em: <https://www.mdpi.com/1424-8220/19/15/3312>.

23 XIONG, J.; CAI, L.; WANG, F.; HE, X. Svm-based spectral analysis for heart rate from multi-channel wppg sensor signals. *Sensors*, v. 17, n. 3, 2017. ISSN 1424-8220. Disponível em: <https://www.mdpi.com/1424-8220/17/3/506>.

24 LAMPOLTSHAMMER, T. J.; FREITAS, E. Pignaton de; NOWOTNY, T.; PLANK, S.; COSTA, J. P. C. L. D.; LARSSON, T.; HEISTRACHER, T. Use of local intelligence to reduce energy consumption of wireless sensor nodes in elderly health monitoring systems. *Sensors*, Multidisciplinary Digital Publishing Institute, v. 14, n. 3, p. 4932–4947, 2014.

25 PRZYBYŁO, J. Continuous distant measurement of the user's heart rate in human-computer interaction applications. *Sensors*, v. 19, n. 19, 2019. ISSN 1424-8220. Disponível em: <https://www.mdpi.com/1424-8220/19/19/4205>.

26 ALLEN, J. Photoplethysmography and its application in clinical physiological measurement. *Physiological Measurement*, v. 28, n. 3, p. R1–39, 2007. Disponível em: <http://stacks.iop.org/0967-3334/28/i=3/a=R01>.

27 BUCCELLETTI, E.; GILARDI, E.; SCAINI, E.; GALIUTO, L.; PERSIANI, R.; BIONDI, A.; BASILE, F.; SILVERI, N. G. et al. Heart rate variability and myocardial infarction: systematic literature review and metanalysis. *Eur Rev Med Pharmacol Sci*, v. 13, n. 4, p. 299–307, 2009.

28 SANTAMARIA, I.; PANTALEON, C.; IBANEZ, J. A comparative study of high-accuracy frequency estimation methods. *Mechanical Systems and Signal Processing*, Elsevier, v. 14, n. 5, p. 819–834, 2000.

29 PROAKIS, J. G. *Digital Signal Processing: Pearson New International Edition*. Pearson Group, 2013. ISBN 1292025735. Disponível em: <https://www.xarg.org/ref/a/1292025735/>.

30 ZHANG, F.; YEDDANAPUDI, M.; MOSTERMAN, P. J. Zero-crossing location and detection algorithms for hybrid system simulation. *IFAC Proceedings Volumes*, v. 41, n. 2, p. 7967 – 7972, 2008. ISSN 1474-6670. 17th IFAC World Congress. Disponível em: <http://www.sciencedirect.com/science/article/pii/S1474667016402296>.

31 SCHOLKMANN, F.; BOSS, J.; WOLF, M. An efficient algorithm for automatic peak detection in noisy periodic and quasi-periodic signals. *Algorithms*, Multidisciplinary Digital Publishing Institute, v. 5, n. 4, p. 588–603, 2012.

32 PRETTZ, J. B.; COSTA, J. P. C. L. da; ALVIM, J. R.; MIRANDA, R. K.; ZANATTA, M. R. Efficient and low cost MIMO communication architecture for smartbands applied to postoperative patient care. In: *2017 Second Russia and Pacific Conference on Computer Technology and Applications (RPC)*. Vladivostok: IEEE, 2017. p. 1–5. ISBN 978-1-5386-3592-6. Disponível em: <http://ieeexplore.ieee.org/document/8168055/>.

33 TEXAS INSTRUMENTS. *CC2640 SimpleLink™Bluetooth® Wireless MCU*. [S.l.], 2016. Rev. B.

34 MAXIM INTEGRATED. *MAX30205 Human Body Temperature Sensor*. [S.l.], 2016. Rev. 0.

35 ROY, R.; KAILATH, T. Esprit-estimation of signal parameters via rotational invariance techniques. *IEEE Transactions on Acoustics, Speech, and Signal Processing*, v. 37, n. 7, p. 984–995, Jul 1989. ISSN 0096-3518.

36 REIS, P. M. G. I.; COSTA, J. P. C. L. da; MIRANDA, R. K.; DEL GALDO, G. Esprit-hilbert-based audio tampering detection with svm classifier for forensic analysis via electrical network frequency. *IEEE Transactions on Information Forensics and Security*, v. 12, n. 4, p. 853–864, April 2017. ISSN 1556-6013.

37 REGA, D. G.; MIRANDA, R. K.; JAVIDI, E.; MARANHÃO, J. P. A.; COSTA, J. P. C. L. da; PINHEIRO, G. P. M. ESPRIT-Based Step Count for Wearable Devices. In: *2019 13th International Conference on Signal Processing and Communication Systems (ICSPCS)*. Gold Coast, Australia: IEEE, 2019. p. 1–5. ISBN 978-1-72812-194-9. Disponível em: <https://ieeexplore.ieee.org/document/9008702/>.

38 REIS, P. M. G. I.; COSTA, J. P. C. L. da; MIRANDA, R. K.; DEL GALDO, G. Audio authentication using the kurtosis of esprit based enf estimates. In: *2016 10th International Conference on Signal Processing and Communication Systems (ICSPCS)*. [S.l.: s.n.], 2016. p. 1–6.

39 MANOLAKIS, D. G.; INGLE, V. K.; KOGON, M. S. *Statistical and Adaptive Signal Processing*. [S.l.]: ARTECH HOUSE, INC., 2005.

40 FERREIRA, H. G. C.; SOUSA JÚNIOR, R. T. de. Security analysis of a proposed internet of things middleware. *Cluster Computing*, Springer, v. 20, n. 1, p. 651–660, 2017.

41 ALMEIDA, M. de; SOUSA JÚNIOR, R. T. de; VILLALBA, L. J. G.; KIM, T.-H. New dos defense method based on strong designated verifier signatures. *Sensors*, MDPI AG, v. 18, n. 9, p. 2813, Aug 2018. ISSN 1424-8220. Disponível em: <http://dx.doi.org/10.3390/s18092813>.

42 MAXIM INTEGRATED. *MAX30100 Pulse Oximeter and Heart-Rate Sensor IC for Wearable Health*. [S.l.], 2014. Rev. 0.

43 MAXIM INTEGRATED. *MAX30102 High-Sensitivity Pulse Oximeter and Heart-Rate Sensor for Wearable Health*. [S.l.], 2018. Rev. 1.

44 SMITH, J. *Introduction to Digital Filters : with audio applications*. United States: W3K, 2008. ISBN 978-0974560717.

45 ASSIS, M. F. P. de. *Implementação de Algoritmos em Sistemas Embarcados de Baixo Consumo Dotados de Rádio Sem Fio e Análise de Perfil de Consumo Energético*. Tese (Trabalho de Conclusão de Curso) — Universidade de Brasília, Faculdade de Tecnologia, Departamento de Engenharia Elétrica, Brasília, DF, 2018.

46 SOKOL, S. Visually evoked potentials: theory, techniques and clinical applications. *Survey of ophthalmology*, Elsevier, v. 21, n. 1, p. 18–44, 1976.

47 HARDING, G. F.; ODOM, J. V.; SPILEERS, W.; SPEKREIJSE, H.; VISION, I. S. for Clinical Electrophysiology of et al. Standard for visual evoked potentials 1995. *Vision research*, Pergamon, v. 36, n. 21, p. 3567–3572, 1996.

48 ZHANG, Y.; XIE, S. Q.; WANG, H.; ZHANG, Z. Data analytics in steady-state visual evoked potential-based brain–computer interface: A review. *IEEE Sensors Journal*, IEEE, v. 21, n. 2, p. 1124–1138, 2020.

49 NOLTE, G.; HOLROYD, T.; CARVER, F.; COPPOLA, R.; HALLET, M. Localizing brain interactions from rhythmic eeg/meg data. In: *26th Annual International Conference of the IEEE EMBS*. [S.l.: s.n.], 2004.

50 PHOTHISONOTHAI, M.; DUAN, H. T. F.; KONDO, A.; AIHARA, K.; YOSHIMURA, Y.; KIKUCHI, M.; MINABE, Y.; WATANABE, K. Artifactual component classification from meg data using support vector machine. In: *The 2012 Biomedical Engineering International Conference (BMEiCON-2012)*. [S.l.: s.n.], 2012.

51 BREUER, L.; DAMMERS, J.; ROBERTS, T. P. L.; SHAH, N. J. A constrained ica approach for real-time cardiac artifact rejection in magnetoencephalography. *IEEE TRANSACTIONS ON BIOMEDICAL ENGINEERING*, v. 61, p. 405 – 414, 2014.

52 HIMBERG, J.; HYVÄRINEN, A. Icasso: software for investigating the reliability of the ica estimates by clustering and visualization. In: *IEEE Workshop on Neural Networks for Signal Processing (NNSP2003)*. [S.l.: s.n.], 2003.

53 AKAIKE, H. A new look at the statistical model identification. *IEEE Trans. on Automatic Control*, v. 19, p. 716 – 723, 1974.

54 WAX, M.; KAILATH, T. Detection of signals by information theoretic criteria. *IEEE Trans. on Acoustics, Speech, and Signal Processing*, 1985.

55 JAVIDI, E. Automatisches framework zum auswahl der komponenten anzahl und zur schätzung der visuell evozierten potentialen komponenten. *Masterthesis, Ilmenau University of Technology*, 2019.

56 KRISHNAIAH, P. R.; ZHAO, L. C.; BAI, Z. D. On detection of the number of signals in presence of white noise. *Journal of Multivariate Analysis*, v. 20, 1986.

57 VIGÁRIO, R.; OJA, E. Bss and ica in neuroinformatics: From current practices to open challenges. *IEEE REVIEWS IN BIOMEDICAL ENGINEERING*, 2008.

58 SHARAFALDIN, I.; LASHKARI, A. H.; GHORBANI, A. A. Toward generating a new intrusion detection dataset and intrusion traffic characterization. In: INSTICC. *Proc. 4th Int. Conf. Inf. Syst. Secur. Privacy - Volume 1: ICISSP*. [S.l.]: SciTePress, 2018. p. 108–116. ISBN 978-989-758-282-0.

59 GITHUB. *February 28th DDoS Incident Report*. 2018. <https://github.blog/2018-03-01-ddos-incident-report/>, Last accessed on 2019-05-14.

60 CISCO. *Cisco Visual Networking Index: Forecast and Trends, 2017–2022*. 2019. <https://www.cisco.com/c/en/us/solutions/collateral/service-provider/visual-networking-index-vni/white-paper-c11-741490.html>, Last accessed on 2020-04-09.

61 MAHJABIN, T.; XIAO, Y.; SUN, G.; JIANG, W. A survey of distributed denial-of-service attack, prevention, and mitigation techniques. *Int. J. Distrib. Sensor Netw.*, v. 13, n. 12, p. 1 – 32, 2017.

62 ZANATTA, M. R.; MENDONÇA, F. L. L. de; ANTREICH, F.; LIMA, D. V. de; MIRANDA, R. K.; DEL GALDO, G.; COSTA, J. P. C. L. da. Tensor-based time-delay estimation for second and third generation global positioning system. *Digit. Signal Process.*, v. 92, p. 1 – 19, 2019. ISSN 1051-2004.

63 GOMES, P. R. B.; COSTA, J. P. C. L. da; ALMEIDA, A. L. F. de; SOUSA JÚNIOR, R. T. de. Tensor-based multiple denoising via successive spatial smoothing, low-rank approximation and reconstruction for R-D sensor array processing. *Digit. Signal Process.*, v. 89, p. 1 – 7, 2019. ISSN 1051-2004.

64 HOSSEINI, S.; AZIZI, M. The hybrid technique for DDoS detection with supervised learning algorithms. *Comput.Netw.*, v. 158, p. 35 – 45, 2019. ISSN 1389-1286.

65 WANG, M.; LU, Y.; QIN, J. A dynamic MLP-based DDoS attack detection method using feature selection and feedback. *Comput. Security*, v. 88, p. 1 – 14, 2020. ISSN 0167-4048.

66 Canadian Institute for Cybersecurity. *NSL-KDD dataset*. 2009. <https://www.unb.ca/cic/datasets/nsl.html>, Last accessed on 2019-06-02.

67 Canadian Institute for Cybersecurity. *DDoS Evaluation Dataset (CICDDoS2019)*. 2019. <https://www.unb.ca/cic/datasets/ddos-2019.html>, Last accessed on 2019-10-02.

68 DAVID, B. M.; COSTA, J. P. C. L. da; FREITAS, E. P. de; SERRANO, A. M. R.; SOUSA JÚNIOR, R. T. de. A parallel approach to PCA based malicious activity detection in distributed honeypot data. *Int. J. Forensic Comput. Sci.*, v. 1, p. 8–27, 2011.

69 COSTA, J. P. C. L. da; FREITAS, E. P. de; DAVID, B. M.; SERRANO, A. M. R.; AMARAL, D.; SOUSA JÚNIOR, R. T. de. Improved blind automatic malicious activity detection in honeypot data. In: *Proc. 7th Int. Conf. Forensic Comput. Sci. (ICoFCS 2012)*. [S.l.: s.n.], 2012. p. 46–55.

70 COSTA, J. P. C. L. da; FREITAS, E. P. de; SERRANO, A. M. R.; SOUSA JÚNIOR, R. T. de. Improved parallel approach to PCA based malicious activity detection in distributed honeypot data. *Int. J. Forensic Comput. Sci.*, v. 2, p. 8–20, 2012.

71 VIEIRA, T. P. B.; TENÓRIO, D. F.; COSTA, J. P. C. L. da; FREITAS, E. P. de; DEL GALDO, G.; SOUSA JÚNIOR, R. T. de. Model order selection and eigen similarity based framework for detection and identification of network attacks. *J. Netw. Comput. Appl.*, v. 90, p. 26 – 41, 2017. ISSN 1084-8045.

72 OSANAIYE, O.; CAI, H.; CHOO, K. R.; DEHGHANTANHA, A.; XU, Z.; DLODLO, M. Ensemble-based multi-filter feature selection method for DDoS detection in cloud computing. *EURASIP J. Wireless Commun. Netw.*, v. 130, p. 1 – 10, 2016.

73 KUSHWAH, G. S.; ALI, S. T. Detecting DDoS attacks in cloud computing using ANN and black hole optimization. In: *2017 2nd Int. Conf. Telecommun. Netw. (TEL-NET)*. [S.l.: s.n.], 2017. p. 1–5.

74 MARANHÃO, J. P. A. *Tensor Based Machine Learning Frameworks for Intrusion Detection in the Physical and Network Layers of Cyber-Physical Systems - Ph.D. dissertation*. [S.l.]: University of Brasília, 2021.

APPENDIX

A CYBERSECURTIY FRAMEWORK

Distributed Denial of Service (DDoS) attacks are one of the most important security threats, since multiple compromised systems perform massive attacks over a victim, overwhelming its bandwidth and/or resources. Such attacks can be detected, for example, by using supervised machine learning based solutions previously trained on large DDoS attack datasets in order to automatically identify malicious patterns present in the incoming traffic. In addition, since large datasets show inherent multidimensional structures, tensor based detection techniques can outperform the matrix based counterparts. In this context, the development of a DDoS attack detection framework which exploits both machine learning and tensor based approaches is crucial. To face this challenge, we summarize three journal publications [5, 6, 7] with contributions on the area of cybersecurity.

Network intrusion detection plays a fundamental role in the process of protecting critical networks by monitoring and analyzing suspicious activities, incidents, threats and violations. In this context, since *Intrusion Detection Systems* (IDS) provide forewarnings about malicious behaviors, such as intrusion attempts and malware, they are used by security administrators in order to detect and countermeasure sophisticated network attacks [58].

DDoS attacks are one of the most important threats to network security. For example, in 2018 the developer platform GitHub was hit by a huge DDoS attack which reached 1.35 terabits per second during a period of 15 to 20 minutes [59]. Additionally, according to the Cisco Annual Internet Report (2018–2023), DDoS attacks correspond to 25 $\%$ of the total Internet traffic of a country during their occurrence [60]. Still according to [60], there will be 14.5 million of DDoS attacks in the world in 2022, implying into major security threats to governments and corporations.

In order to launch DDoS attacks into target systems, hackers can make use of legitimate third part components (normally web servers) through the combined effort of thousands of compromised machines known as “zombies”. Such zombies establish a “zombie network” that exhausts victim’s bandwidth or resources through a massive traffic attack, while hiding the attacker’s identity. Moreover, the weaknesses of different network layer protocols are exploited by an attacker and, consequently, the victim uses huge CPU and memory resources to process intensive operations [61].

In this sense, it is fundamental that network administrators adopt accurate and efficient schemes in order to detect and prevent DDoS attacks in their organizations. For instance, tensor based signal processing techniques have attracted an increasing attention in the last years since they allow us to better exploit the inherent multidimensional structure of large datasets [62, 63]. Furthermore, supervised ML based methods can provide an efficient way

to detect DDoS attacks [64, 65]. As ML algorithms can be trained on benchmark datasets provided by cybersecurity institutes [66, 67], such schemes can be used to identify, with high reliability, malicious patterns eventually present in the input network traffic in an automated fashion.

To face the challenge of DDoS attack detection, schemes based on traditional signal processing techniques have attracted a great attention in the last decades. A MOS technique for blind automatic malicious activity detection in distributed honeypots was proposed by David et al. in [68], where human intervention or information about attacks were not required. In line with the ideas of [68], Da Costa et al. proposed a blind automatic scheme to detect malicious traffic in network data collected at honeypot systems [69] as well as the R-D Akaike Information Criterion and the R-D Minimum Description Length to automatically identify malicious activities in honeypots [70]. In addition, it is worth to mention the recent work of Vieira et al., which proposed a framework in order to detect the number of port scanning and flood attacks by analyzing the largest eigenvalues in time frames after applying MOS and similarity analysis on the dataset [71]. However, since the approaches in [68]-[71] are not tensor based solutions and do not consider automatic learning, we fill those gaps by exploiting the inherent tensor structure present in large datasets as well as by applying classic machine learning classification algorithms such that the proposed technique learns to recognize patterns in multidimensional data.

Finally, ML based schemes have also been successfully used for DDoS attack detection. Osanaiye et al. [72] presented an ensemble based multi-filter feature selection method for DDoS attack detection in cloud computing where the output of filter methods are combined to achieve an optimum selection. Furthermore, a model based on artificial neural networks and black hole optimization algorithm to detect DDoS attacks in cloud computing was presented in [73]. Moreover, in [64], the authors proposed a hybrid framework based on data stream approach for DDoS attack detection where the computational load is divided between the client and proxy side. Finally, Wang et al. proposed to combine feature selection with multilayer perceptron to select the optimal features as well as designed a feedback mechanism to perceive detection errors dynamically [65]. Thus, despite the machine learning based schemes proposed by [64], [65], [72] and [73] show high performance in terms of DDoS attack detection, they did not exploit multidimensional techniques. Therefore, we also fill such research gap by adopting and extending tensor based denoising approaches, particularly the recent MuDe scheme, such that the inherent tensor structure of large datasets can be exploited more efficiently.

Since tensor based signal processing techniques as well as machine learning based algorithms have shown high performance when considering large datasets and network intrusion detection problems, respectively, we propose a novel framework for DDoS attack detection which exploits both approaches. The proposed architecture is composed by four steps:

data preprocessing, dataset splitting, dataset denoising and machine learning classification. Moreover, in the third step we propose an extension of the recent MuDe technique, which attenuates the noise present in the dataset instances. Experiments show that the proposed framework achieves satisfactory performance, with outstanding values of accuracy, detection rate and false alarm rate when compared with traditional low-rank approximation techniques as well as with related works.

Hence, the major contributions of [5] are summarized as follows:

- a novel architecture that combines the benefits of both multidimensional signal processing techniques and supervised machine learning classification algorithms with the aim of providing accurate and efficient DDoS attack detection.
- a recent multidimensional noise reduction technique known as MuDe in order to attenuate the noise present in the instances of DDoS attack detection datasets. The traditional MuDe was proposed by Gomes et al. in [63] and originally was intended to reduce the noise level in measurement data collected by multidimensional sensor arrays in radio communication systems. Our proposed extension is based on two main factors: (i) the application of the traditional MuDe directly on the dataset instances, and (ii) the inclusion of a second denoising stage performed by *Higher Order Orthogonal Iteration* (HOOI) low-rank approximation such that a higher degree of noise reduction is achieved, with significant gain on the overall DDoS attack detection performance. We refer to [74] in order to have more details about these contributions.

B ALGORITHMS OF THE MULTI-SENSOR HEALTH WEARABLE DEVICE FRAMEWORK

In this Appendix, four algorithms used on the multi-sensor health wearable device framework are presented. The first algorithm is a FFT-based HR estimator, while the second algorithm is autocorrelation-based HR estimator. For the step counting, the third and fourth algorithms for frequency estimation by counting zero crossings and peak detection using maximum value in a given interval are shown.

Algorithm 2: FFT-based HR estimator

1 Given signal $x[n]$, sampled with frequency f_s, during a time window T:

2 Form the zero-padded signal by appending $N - T \cdot f_s$ zeros at its end, totaling N points. The achieved frequency resolution is given by f_s/N.

3 Calculate the N-point FFT of the signal and its corresponding frequency arguments.

4 Calculate the absolute value of the frequency domain representation:

$$|X(f)| = \left| \sum_{n=0}^{N-1} x[n] e^{-j2\pi f n/N} \right|$$

Calculate the vector f of length N corresponding to frequency values from 0 to f_s:

$$f = [0,\ f_s/N,\ 2f_s/N, \ldots,\ f_s]$$

5 Compute the frequency argument corresponding to maximum amplitude of the FFT from half the spectrum $0 \leqslant k \leqslant N/2$:

$$\widehat{f} = \underset{0 \leqslant n \leqslant N/2}{\arg\max} |X(f)|$$

Calculate the estimated BPM value form $\widehat{f}$:

$$\text{estimated BPM} = \widehat{f} \cdot 60$$

Algorithm 3: Autocorrelation-based HR estimator

1 Given signal $x[n]$, sampled with frequency f_s, during a time window T:

2 Compute the autocorrelation of the signal for $l \geqslant 0$:

$$r_{xx}[l] = \sum_{n=0}^{T \cdot f_s} x[n]x[n-l], \qquad l = 0, 1, 2, \ldots,$$

3 For $l \neq 0$, compute the lag corresponding to the maximum argument of $r_{xx}[l]$:

$$l_p = \arg\max_{l \geqslant 0}(r_{xx}[l]); \tag{B.1}$$

4 Calculate the frequency estimator $\widehat{f}$ form l_p:

$$\widehat{f} = \frac{1}{l_p}; \tag{B.2}$$

Calculate the estimated BPM value form $\widehat{f}$:

$$\text{estimated BPM} = \widehat{f} \cdot 60. \tag{B.3}$$

Algorithm 4: Frequency estimation by counting zero crossings

1 Given signal $x[n]$, sampled with frequency f_s, during a time window T:

2 Compute the number of zero-crossings in the signal during T according to:

$$z(x) = \begin{cases} 1 & \text{if } x[n] < 0 \text{ and } x[n-1] < 0 \\ 1 & \text{if } x[n] > 0 \text{ and } x[n-1] < 0 \\ 1 & \text{if } x[n] > 0,\ x[n-1] = 0 \text{ and } x[n-2] < 0 \\ 1 & \text{if } x[n] < 0,\ x[n-1] = 0 \text{ and } x[n-2] > 0 \\ 0, & \text{otherwise.} \end{cases}$$

3

$$\text{zero-crossings} = \sum_{n=0}^{T \cdot f_s} z(x[n])$$

Divide the number of zero crossings by during T by 2;

4 Calculate the frequency estimator from half the number of zero crossings during T:

$$\widehat{f} = \frac{\text{zero-crossings}/2}{T};$$

5 Calculate the estimated BPM value form $\widehat{f}$:

$$\text{estimated BPM} = \widehat{f} \cdot 60. \tag{B.4}$$

Algorithm 5: Peak detection using maximum value in a given interval

1 Given signal $x[n]$, sampled with frequency f_s, during a time window T:

2 Find the number of local peaks, in order to detect only the PPG signal's feet during interval T;

3 Calculate the frequency estimator from the sample interval:

$$\widehat{f} = \frac{\text{number of peaks}}{T};$$

4 Calculate the estimated BPM value form $\widehat{f}$:

$$\text{estimated BPM} = \widehat{f} \cdot 60.$$

C STEP COUNTER

To improve medical follow-up despite limited hospital space and resources, wearable tech offers remote patient monitoring. A microelectronic system tracks vital health parameters. This study assesses angular movement in three axes, exploring sensor placement's impact on step detection. Different algorithms like FFT analysis and ESPRIT are compared for accuracy, showing ESPRIT's enhanced step detection capability compared to traditional methods.

Advancements in small-scale hardware and the availability of electronic sensors have fueled the expansion of *Internet of Things* (IoT), enhancing everyday products like fridges, lamps, and watches. Wearable tech, using microcontrollers, now measures vital parameters like temperature, pressure differentials, and heart rate, enabling real-time patient data monitoring. Physical activity significantly affects health, influencing body motion and sports participation, highlighting its relevance in patient well-being.

This study uses step count as an indicator of physical activity, employing gyroscope or accelerometer data to detect steps during walking. By analyzing acceleration and angular velocity, a step-counting method called ESPRIT is proposed and compared to FFT-based approaches. ESPRIT performs better when sensors are on the user's wrist and during slower walking speeds with lower signal amplitude. This finding holds significance for treatments like home-based physiotherapy for neurological diseases, emphasizing the importance of patient adherence to low-speed walking exercises. Remote assessment via the proposed step-counting algorithm could enhance treatment outcomes. Note that the state-of-the-art as well as the the ESPRIT based approaches are explained in the Appendix B.

In Figure C.1, the performance of the step counter algorithms are compared. The proposed ESPRIT based approach for the estimation of the amount of steps outperforms the state-of-the-art schemes.

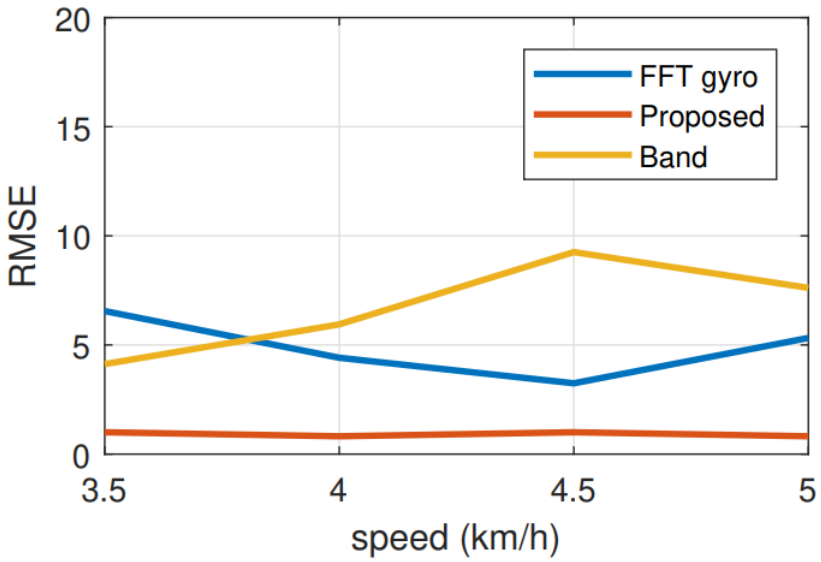

Figure C.1 – The proposed ESPRIT based approach for the estimation of the amount of steps outperforms the state-of-the-art schemes.

D DRONE LOCALIZATION IN MULTIPATH ENVIRONMENTS

The application of drones, or Unmanned Aerial Vehicles (UAVs), across commercial and public safety domains has raised pertinent security concerns pertaining to potential exploitation for espionage and terrorism. Addressing these concerns, we propose a novel framework employing a multidimensional antenna array system to precisely localize UAVs within complex multipath environments. Expanding upon an existing signal emitter localization framework, our approach introduces two key enhancements. Firstly, we leverage tensor representation to effectively exploit the inherently multidimensional nature of the data. Secondly, we integrate a multifaceted denoising preprocessing scheme aimed at augmenting the signal-to-noise ratio in received signals. Numerical analyses and simulations demonstrate the efficacy of our proposed methodology.

Recent studies propose diverse strategies for precise drone localization. These span from utilizing image sensors for azimuth and elevation angle measurements to the development of *Time Difference of Arrival* (TDoA) algorithms and integrated anti-drone systems combining surveillance and jamming functionalities. Some approaches leverage arrays of directional antennas to estimate DoA and localize drones by exploiting specific signal characteristics like NTSC or RSS. However, prevalent high-resolution frameworks exhibit limitations in multidimensional scenarios. Addressing this, an innovative extension adopts tensor representation and a MuDe scheme, showcasing superior performance in drone localization simulations compared to conventional matrix and tensor-based methods with spatial smoothing.

In Figure D.1, we present the Root Mean Squared Error of the estimated spatial frequency versus number of antennas per dimension. The following parameters are considered in the scenario signal-to-interference ratio SIR = 20 dB and SNR = 30 dB, number of signal samples $N = 10$, number of drones within the system $Q = 2$, number of uniform rectangular arrays (URA) $U = 4$, distance between the URA $\delta = 400$ m and amount of *Line of Sight* (LOS) and *Non Line of Sight* (NLOS) components $D = 6$. According to Figure D.1, the proposed MuDe based approach for the estimation of the position significantly outperforms the state-of-the-art schemes.

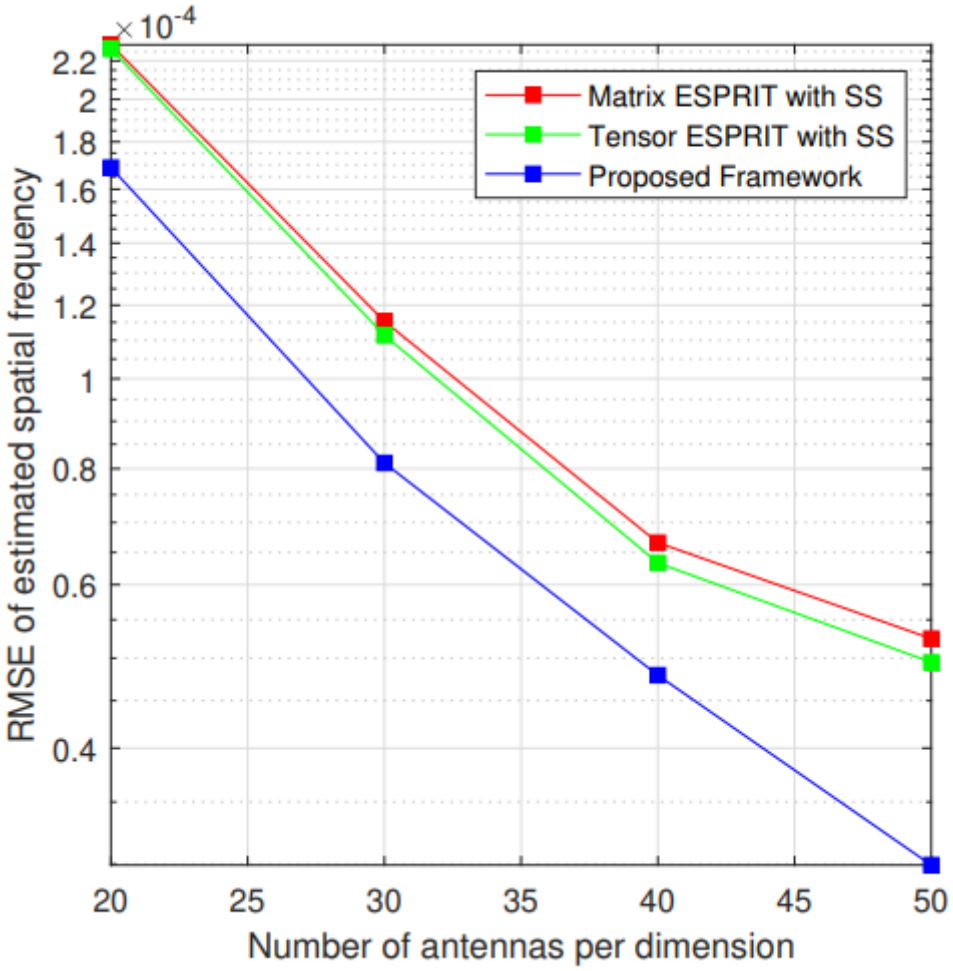

Figure D.1 – The proposed MuDe based approach for the estimation of the position outperforms the state-of-the-art schemes.